PHILOSOPHICAL TRANSACTIONS OF THE ROYAL SOCIETY A
MATHEMATICAL, PHYSICAL & ENGINEERING SCIENCES

X-Ray Analysis of Mesoscopic Twin Structures

K. R. Locherer, S. A. Hayward, P. J. Hirst, J. Chrosch, M. Yeadon, J. S. Abell and E. K. H. Salje

Phil. Trans. R. Soc. Lond. A 1996 **354**, 2815-2845
doi: 10.1098/rsta.1996.0131

X-ray analysis of mesoscopic twin structures

By K. R. Locherer[1,2], S. A. Hayward[1], P. J. Hirst[3],
J. Chrosch[1,2], M. Yeadon[3], J. S. Abell[3] and E. K. H. Salje[1,2]

[1] *Department of Earth Sciences, University of Cambridge,*
Downing Street, Cambridge CB2 3EQ, UK
[2] *IRC in Superconductivity, University of Cambridge,*
Madingley Road, Cambridge CB3 0HE, UK
[3] *School of Metallurgy and Materials, The University of Birmingham,*
Birmingham B15 2TT, UK

This review summarizes recent progress in the use of X-ray diffraction for microstructural investigations. Advances in both detector architecture and computational power have led to the development of powerful yet relatively straight forward methods of analysis. Several case studies are presented.

1. Introduction

Considerable effort has been devoted to computer modelling of microstructural phenomena in ferroelastics such as the high temperature superconductor $YBa_2Cu_3O_{7-\delta}$ and the mineral feldspar. This has so far not been matched by equivalent efforts in experimental observations. A large body of information exists for transmission electron microscopy (Lacayo *et al.* 1992; Putnis & Salje 1994; Schmahl *et al.* 1989; Semenovskaya *et al.* 1993; Van Tendeloo *et al.* 1990, 1995; Zhu & Cowley 1994; Zhu *et al.* 1990, 1991, 1993) but this technique allows only for very limited regions of a sample to be investigated. Furthermore, it does not allow for the quantitative analysis of strain fields generated by mesoscopic structures nor a quantitative analysis of the internal structure of a twin wall boundary. In contrast, X-ray diffraction averages the local structural information over large volumes of the crystal, thus giving more reliable insights into the microstructure within macroscopically sized regions. Such analysis is a prerequisite for all subsequent studies which are based on a thermodynamic treatment of a phase transition. Of particular importance is the diffuse scattering in between Bragg reflections generated by such structures as domain walls. In this review it is shown that copious information can be extracted using, by now, routine methods of investigation. Results include the thickness of domains walls in single crystals and their temperature dependence, the mosaicity of thin films, the spontaneous strain, grain size and domain size. This information is particularly important for wall-related superconductivity and pinning of magnetic flux lines, whereas in minerals it enables conclusions to be drawn on the thermal (geological) history of samples.

Phil. Trans. R. Soc. Lond. A (1996) **354**, 2815–2845
Printed in Great Britain

TEX Paper

2. Microstructures: twins and tweed

The development of certain microstructures is the result of a phase transition from a high-temperature paraelastic phase to a low-temperature ferroelastic phase. Loss of symmetry due to the phase transition is, in most cases, associated with the generation of a spontaneous strain, which in turn leads to the formation of domains. An order parameter can be assigned that will vary from one type of domain to another, and this parameter is a function of temperature, pressure and composition. The dependence of the order parameter on these intensive values is determined by the nature of the phase transition.

Landau (Landau & Lifshitz 1980) first assumed that in the vicinity of a phase transition the Gibbs free energy can be expanded as a Taylor series in terms of the order parameter Q:

$$L(Q) = \sum_{n=0}^{\infty} a_n Q^n. \tag{2.1}$$

Even though strictly speaking the range of temperatures in this perturbation approach is limited, it is found in experiments that in many cases the expansion yields a correct description of thermodynamical behaviour over many hundreds of degrees K (Salje 1990). Later it was found that the expression for $L(Q)$ in (2.1) is the result of the collective interaction of interatomic potentials, which are indeed well described by polynomial expressions. In this sense, $L(Q)$ is *not* only a simple Taylor expansion of the true Gibbs free energy $G(Q)$, but the expression for $L(Q)$ follows directly from the full analysis of the local interatomic interactions (Salje *et al.* 1991).

For a second-order phase transition, terms of order two, four and six are involved (Salje 1990):

$$L(Q) = \tfrac{1}{2}A(T - T_c)Q^2 + \tfrac{1}{4}BQ^4 + \tfrac{1}{6}CQ^6. \tag{2.2}$$

The total Gibbs free energy is now given by the Landau energy plus the elastic energy from the relaxation of the unit cell given by the spontaneous strain and a coupling term between the spontaneous strain and the order parameter:

$$G(Q,e) = \tfrac{1}{2}A(T - T_c)Q^2 + \tfrac{1}{4}BQ^4 + \tfrac{1}{6}CQ^6 + \tfrac{1}{2}\sum_{ijlm} c_{ijlm}e_{ij}e_{lm} + \sum_{mn} \xi_{imn}e_i^m Q^n. \tag{2.3}$$

Any change in the order parameter must induce lattice strains, and vice versa. Thus Q and e are not independent but couple. Considering bilinear coupling (Salje 1990; Tsatskis *et al.* 1994) one finds (ignoring Q^6)

$$G(Q,e) = \tfrac{1}{2}A(T - T_c)Q^2 + \tfrac{1}{4}BQ^4 + \tfrac{1}{2}\sum_{ik} c_{ik}e_i e_k + \sum_{i} \xi_i e_i Q, \tag{2.4}$$

where c_{ik} are the elastic constants in Voigt notation. The equilibrium order parameter is obtained by minimizing the Landau free energy with respect to e and Q:

$$\frac{\partial G}{\partial e_i} = \frac{1}{2}\sum_{k} c_{ik}e_k + \xi_i Q \tag{2.5}$$

$$= 0. \tag{2.6}$$

It immediately follows that the spontaneous strain is linearly proportional to the order parameter (Salje 1990):

$$e_i = M_i(c_{ik}, \xi_i)Q. \tag{2.7}$$

Also one finds that the transition temperature is renormalized such that

$$T_c^* = T_c - \frac{1}{A}\left(\sum_{ik} c_{ik} M_i M_k + 2\sum_i \xi_i M_i\right), \tag{2.8}$$

where M_i follows from (2.7). The Gibbs free energy is then given by

$$G(Q) = \tfrac{1}{2}A(T - T_c^*)Q^2 + \tfrac{1}{4}BQ^4 + \tfrac{1}{6}CQ^6. \tag{2.9}$$

Now this free energy expression should be minimized with respect to Q to get the equilibrium order parameter, and neglecting the sixth-order term

$$\frac{\partial G}{\partial Q} = A(T - T_c^*)Q + BQ^3 \tag{2.10}$$

$$= 0. \tag{2.11}$$

Thus the order parameter varies as the square root of temperature:

$$Q = \begin{cases} \sqrt{(A/B)(T_c^* - T)}, & T < T_c^*, \\ 0, & T > T_c^*. \end{cases} \tag{2.12}$$

In principle the same type of analysis can be performed for variations in impurity concentrations. This is based on the consideration that the behaviour of the end-member (here $\mathrm{YBa_2Cu_3O_{7-\delta}}$) is generally known, and the effect of a solute can be added by introducing a coupling term between the solute concentration and the order parameter of the solvent.

One can thus modify the above calculations to include the effect of compositional changes:

$$G(Q, X) = \tfrac{1}{2}A(T - T_c)Q^2 + \tfrac{1}{4}BQ^4 + \tfrac{1}{6}CQ^6 + \cdots + mXQ + nXQ^2 + \cdots. \tag{2.13}$$

For symmetry reasons we shall assume that $m = 0$ (Carpenter 1992; Salje 1990), such that one finds

$$G(Q, X) = \tfrac{1}{2}A(T - T_c')Q^2 + \tfrac{1}{4}BQ^4 + \tfrac{1}{6}Q^6 + \cdots, \tag{2.14}$$

where $T_c' = T_c - (2n/A)X$. Thus the coupling of the order parameter with composition also renormalizes the transition temperature. Performing the same minimization procedures to $G(Q, X)$ as above,

$$\frac{\partial G}{\partial Q} = A\,(T - T_c')\,Q + BQ^3, \tag{2.15}$$

$$= 0, \tag{2.16}$$

gives the variation of the order parameter with X as

$$Q = \sqrt{\frac{A}{B}\left(T_c - T - \frac{2n}{A}\right)} \tag{2.17}$$

$$= \sqrt{\frac{A}{B}\,(T_c' - T)}. \tag{2.18}$$

However, this simplified approach gives a linear dependence of T_c on the concentration, whereas in fact one observes the following two distinct regimes (Salje 1990, 1995; Hayward & Salje 1995; Carpenter 1992).

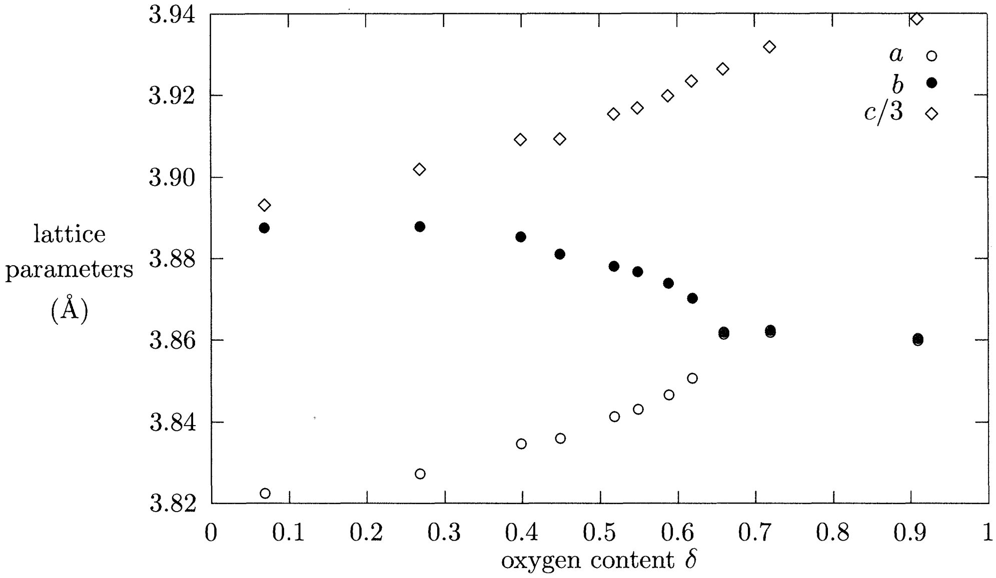

Figure 1. Variation of lattice constants with oxygen content δ in $YBa_2Cu_3O_{7-\delta}$. Taken from Jorgensen *et al.* (1990).

(i) When the impurity concentration is very low the resulting strain fields do not overlap, leading only to local phase transitions within small volumes around the defect, only weakly affecting the bulk. The overall T_c will be only weakly affected by this, and this region is the called the plateau effect.

(ii) When the impurity concentration becomes large enough the strain fields due to the defects do overlap, leading to a change in the macroscopic transition temperature and transformation. This is equivalent to chemical mixing.

In general materials are not structurally homogeneous but exhibit a variation on a mesoscopic scale (Salje 1990). The inhomogeneities averaged over several lattice sites will then give the macroscopic order parameter. In reciprocal space this corresponds to non-zero wavevectors for the modulations. This can be incorporated into the Landau free energy such that

$$G(Q) = \tfrac{1}{2}A(T - T_c)Q^2 + \tfrac{1}{4}BQ^4 + \tfrac{1}{2}g(\nabla Q)^2. \tag{2.19}$$

When solving this equation for equilibrium it is found that the structure contains domain walls separating regions of order parameters having opposite signs. The variation of the order parameter across the domain boundary is described in a second-order phase transition by (Salje 1990)

$$Q = Q_0 \tanh(r/w), \tag{2.20}$$

where r is the distance perpendicular to the domain wall. Theory predicts a wall thickness w of

$$w = \sqrt{\frac{4}{3}\frac{gT_c}{A|(T - T_c)/T_c|}} \propto \frac{1}{Q}. \tag{2.21}$$

Thus w decreases with decreasing temperature as one would expect, since the energy difference between the low-temperature phase, in the bulk, and the high-temperature phase, associated with the wall, increase with decreasing temperature. Decreasing the

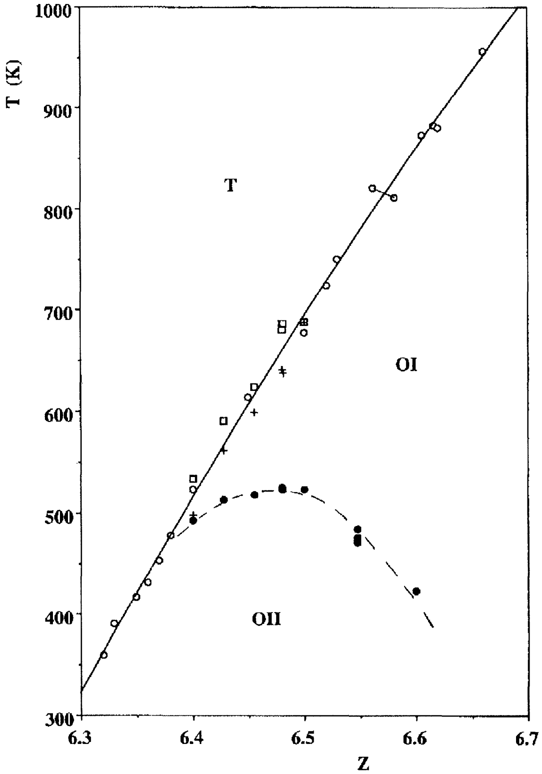

Figure 2. Structural phase diagram of $YBa_2Cu_3O_z$. T stands for tetragonal, while *OI* and *OII* refer to orthorhomic structure O(I) ($a_0 \times a_0$) and O(II) ($a_0 \times 2a_0$), respectively. Reprinted from Gerdanian & Picard (1993) with the kind permission of Elsevier Science – NL, Sara Burgerhartstraat 25, 1055 KV Amsterdam, The Netherlands.

wall thickness is the only way, other than the destruction of the wall, for the crystal to reduce the excess energy spent on the microstructure. Towards the transition temperature, w diverges, i.e. the high-symmetry phase spreads through the whole crystal at an infinite rate from within the walls (Salje 1990).

The term ‘tweed’ describes a diffraction pattern observed in transmission electron microscopy (TEM) in many different materials, such as in memory shape alloys (NiAl, FePd, CuAu (Kartha *et al.* 1995)), minerals (aluminosilicates, $KAlSi_3O_8$, $Mg_2Al_4Si_5O_{18}$ (Putnis & Salje 1994)) and high-temperature superconductors ($YBa_2Cu_3O_{7-\delta}$ and La_2CuO_4 (Kartha *et al.* 1995)). It bears close resemblance to the textile and hence its name. We shall use the superconductor $YBa_2Cu_3O_{7-\delta}$ as an example to illustrate tweed and exclude tweed generated by spinodal decomposition. $YBa_2Cu_3O_{7-\delta}$ is essentially made up of three perovskite unit cells $a_0 \times a_0 \times 3a_0$, $a_0 \sim 3.8$ Å being the perovskite lattice parameter. The underlying physical concept to the order parameter in $YBa_2Cu_3O_{7-\delta}$ is given by the arrangement of oxygen atoms in the basal plane of the unit cells. When changing δ in $YBa_2Cu_3O_{7-\delta}$ from zero to 1 the symmetry of the unit cell changes from orthorhombic to tetragonal (figure 1). The lattice constants in the x–y plane depend crucially on whether an oxygen atom takes the space between the two copper atoms or not, and this is the physical reason why the strain and the order parameter must couple.

A structural phase diagram is given in figure 2. The tetragonal phase denoted by T is paraelastic. The precise structure of this region is subject to ongoing debates (see later). The other two fields, $O(\mathrm{I})$ and $O(\mathrm{II})$ (Schleger *et al.* 1995*a*), are orthorhombic and ferroelastic. In $O(\mathrm{I})$ copper–oxygen chains are formed along either (100) or (010), giving domains with two possible variants of the order parameter. This is the microscopic origin of twinning. $O(\mathrm{II})$ also consists of copper–oxygen chains. The difference between $O(\mathrm{II})$ and $O(\mathrm{I})$ is that chains are separated by two lattice constants. Not represented in the diagram is yet another orthorhombic phase, $O(\mathrm{III})$ (Schleger *et al.* 1995*b*), in which the chains are separated by three lattice constants. Various other superstructures have been reported, such as $2\sqrt{2}a_0 \times 2\sqrt{2}a_0$ (Semenovskaya & Kachaturyan 1992).

Transmission electron microscopy has been extensively used to investigate $\mathrm{YBa_2\,Cu_3O_{7-\delta}}$, as cited in the Introduction. Three length scales in this quasi-periodic structure are of importance: the longitudinal extent and the relatively short transverse width, giving a poorly defined overall wavevector. It is generally agreed that the latter is of the order of 40–100 Å.

To explain tweed, let us consider two cases. One is fully oxygenized $\mathrm{YBa_2Cu_3O_7}$ and the other is oxygen deficient $\mathrm{YBa_2Cu_3O_{7-\delta}}$. In both cases long-range elastic interactions form the key to understanding tweed. When atomic ordering takes place in one unit cell of the crystal it inevitably pulls or pushes atoms and thus creates a local displacement field, which in turn generates its own displacement field. Thus there is an indirect ordering interaction $J(\boldsymbol{R}_{ij})$ in the material mediated by strain (Bratkovsky *et al.* 1995).

(i) $\mathrm{YBa_2Cu_3O_{7-\delta}}$ *with* $\delta = 0$

The existence of kinetic tweed is caused by non-equilibrium thermodynamics in samples below the transition temperature. When annealed at a temperature below T_c this tweed, consisting of an assembly of microdomains, coarsens to form intersecting domains along $\langle 110\rangle$ and $\langle 1\bar{1}0\rangle$ due to the long-range elastic interactions. Since the intersections cost elastic energy, needle-shaped domains form and the needle tips subsequently retract until the whole crystal matrix is transformed into a series of parallel twins called ‘stripes’. At this point the kinetic process comes to a halt. Embryos of tweed structure are found at temperatures up to $2T_\mathrm{c}$ in this theory, which is based both on computer simulations using combined molecular dynamics–Monte Carlo methods and analytical solutions of long-range elastic interactions. All other interactions are taken to be negligible (e.g. screened Coulomb). The analytical solutions consider a very general form of interactions, irrespective of the detailed atomic configuration of a given material of the type

$$J(\boldsymbol{R}) \sim \frac{A_2Y_{2m}(\theta,\phi) + A_4Y_{4m}(\theta,\phi)}{R^3} + J_\mathrm{Z}, \tag{2.22}$$

$$J_\mathrm{Z} = \frac{Z}{N}, \tag{2.23}$$

for ferroelastics and

$$J(\boldsymbol{R}) \sim \frac{A_2Y_{2m}(\theta,\phi) + A_4Y_{4m}(\theta,\phi) + A_6Y_{6m}(\theta,\phi)}{R^5} \tag{2.24}$$

for antiferroelastics. Y_{lm} are spherical harmonics of order two, four and six, and J_Z is an infinite range Zener–Eshelby-type force (Bratkovsky *et al.* 1994*a*, *c*, 1995; Putnis & Salje 1994; Salje & Parlinski 1991; Parlinski *et al.* 1993*a*, *b*).

(ii) $YBa_2Cu_3O_{7-\delta}$ *with* $\delta > 0$

Developments of microstructure in this model were studied by solving the crystal lattice diffusion equation

$$\frac{\mathrm{d}c_p(\boldsymbol{r},t)}{\mathrm{d}t} = \sum_{q=1}^{q=2}\sum_{\boldsymbol{r}'} L(\boldsymbol{r}-\boldsymbol{r}')_{pq}\frac{\delta F}{\delta c_q(\boldsymbol{r}',t)}, \tag{2.25}$$

where a Bragg–Williams type of the free-energy functional is used for F, $c_p(\boldsymbol{r},t)$ is the distribution function and $L(\boldsymbol{r}-\boldsymbol{r}')_{pq}$ is the matrix of kinetic coefficients, for square lattices of 64 × 64 or 128 × 128 unit cells. Similar results to the case of $\delta = 0$ were found. One obvious difference is that here one can end up in various orthorhombic phase fields such as O(I) or O(II) (figure 2). The rate of quenching decides which phase is the end product. The phase diagram is well reproduced (Semenovskaya & Kachaturyan 1991, 1992, 1993; Semenovskaya *et al.* 1993).

For completeness we mention an attempt by Kartha *et al.* (1995) to develop a theory of tweed in which fluctuations are promoted by the lattice geometric constraints to form a frustrated glassy phase.

We consider the case of fully oxygenized $YBa_2Cu_3O_7$ here since it has the highest transition temperature and is thus most useful to applications. Using a simpler yet less general and fully analytical approach than in (2.23) and (2.24) leads to a modified Ornstein–Zernike result (Vul *et al.* 1995). It shows that tweed might arise from a strongly anisotropic correlation of oxygen atoms in equilibrium at temperatures well above T_c, with fluctuations in the order parameter becoming critical along the 'soft' $\langle 110\rangle$ and $\langle 1\bar{1}0\rangle$ directions as the transition temperature is approached. Tweed in this model is described as a short-range order phenomenon in thermodynamic equilibrium, and no microdomains are needed to explain the typical 'butterfly'-shaped X-ray diffraction pattern. It is speculated that since oxygen diffusion at temperatures well below T_c is very slow it might be expected that the prequenching microstructure is simply 'frozen in' (Vul *et al.* 1995).

All models have in common the fact that $YBa_2Cu_3O_{7-\delta}$ is considered to be essentially two dimensional, with relevant interactions taking place between the copper and oxygen atoms of the basal plane only. The reason for being able to reduce the problem to two dimensions is that the distance between the (001) planes is about three times that between the (100) planes, and as a result diffusion is about 10^{-6} times less likely to take place between the former (Semenovskaya & Kachaturyan 1993). In the temperature range of interest diffusion is effectively limited to the oxygen atom, with the cations (copper in the undoped case) frozen in. Long-range Coulomb interactions will prevent any clustering of charges of equal signs. To preserve charge homogeneity it is thus only possible to redistribute the oxygen atoms on the interstitial sites.

We discuss now the role of incorporation of other ions into the host matrix of $YBa_2Cu_3O_{7-\delta}$. Various ions can be substituted into $YBa_2(Cu_{1-x}M_x)_3O_{7-\delta}$. It is found that M = Al, Fe, Ga and Co are preferentially exchanged for divalent Cu(I) (Kistenmacher 1988). This is because the trivalent dopands prefer octahedral coordination, and the Cu(I) sites have a larger number of oxygen atoms around them than the Cu(II) sites. The effect of adding these dopands is to induce an orthorhombic to tetragonal phase transition at a critical concentration x_c, since they cause a local distortion of the lattice and will attract more oxygen atoms to the basal plane. When the number of dopands becomes large enough for the local strain fields to overlap,

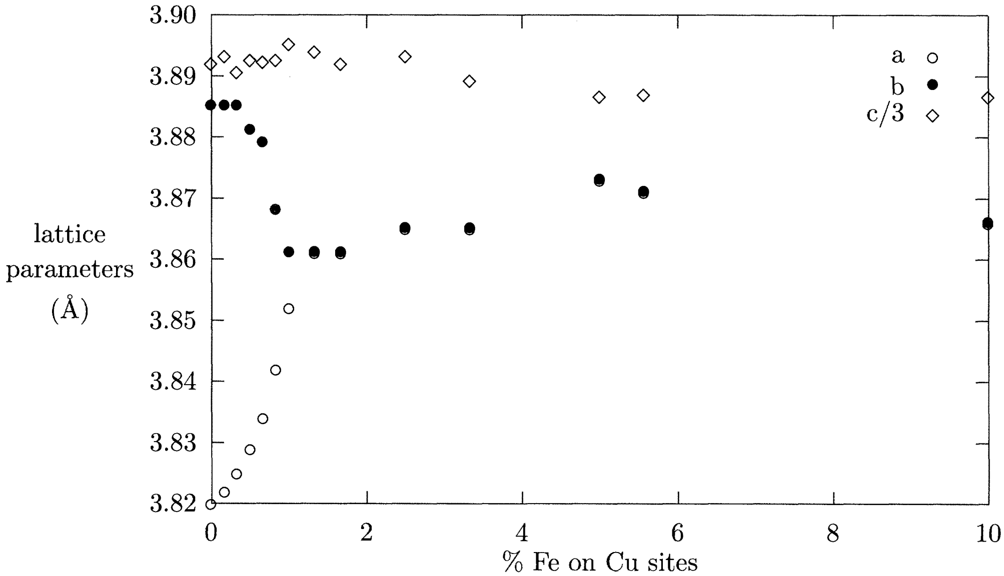

Figure 3. Variation of lattice constants with Fe concentration in $YBa_2Cu_3O_{7-\delta}$. Data taken from Xu *et al.* (1989).

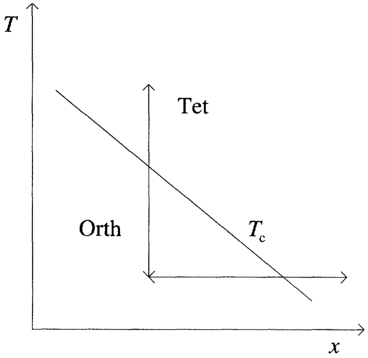

Figure 4. Second order phase diagram of temperature T versus chemical concentration x for bilinear coupling.

the transformation to a macroscopically tetragonal phase takes place. An example of such a transformation is shown for the case of Fe in figure 3. In TEM pictures the twin-to-tweed transition by doping with cobalt is observed as the following sequence (Schmahl *et al.* 1989)

(i) Coarse parallel twins for undoped samples.
(ii) Decreasing domain width with increasing doping concentration.
(iii) Intersecting domains forming 'needles'.
(iv) Cross-hatched tweed with domain size becoming smaller and smaller.

The mean twin spacing decreases asymptotically with increasing cobalt content, with the spontaneous strain dropping to zero following a power law as expected for a second-order phase transition. The c lattice parameter is constant with respect to doping concentration, in contrast to the variation of c with oxygen concentration δ (figure 1).

In experimental studies of tweed it is found that rather than varying temperature it is more sensible to introduce dopands into $YBa_2(Cu_{1-x}M_x)_3O_{7-\delta}$, changing x as in figure 4 while keeping T constant. If one changes T for constant x, $YBa_2Cu_3O_{7-\delta}$ will loose oxygen, making the experimental procedure to counter this oxygen loss extremely difficult and unreliable.

Tweed is observed when the extinction rule

$$\boldsymbol{G} \cdot \boldsymbol{q} = 0 \tag{2.26}$$

is satisfied, giving the typical four-fold 'butterfly' patterns around (hkl), $h \neq k$, and two-fold streaks about (hhl) in X-ray and electron diffraction experiments. $\boldsymbol{G}$ is the reciprocal lattice vector of the Bragg peak, and the origin of $\boldsymbol{q}$.

3. X-Ray diffraction

X-ray diffraction is an extremely valuable tool for analysing microstructures.

(i) It is non-destructive.

(ii) It averages over large areas of material whereas electron microscopy tends to sample limited regions.

(iii) It is sensitive to defects and impurities.

(iv) It is a relatively straight-forward technique.

It was seen as useful to find new ways of employing X-ray diffraction to this end, especially to complement the large amount of theoretical and computational work that has been performed in this field. In particular, thin films have so far been subjected to only relatively simple investigations. This study represents an attempt to gain a solid experimental grounding of the elementary physics of such structures. The many potential applications of these materials make such a study vital.

4. Experimental techniques

The recent explosive progress in both computing and X-ray detector technology has lead to extremely powerful systems that can sample large regions of reciprocal space on a fully automated scale. While the traditional one-channel-detector four-circle machines have been controlled by entering the desired volume in units of the reciprocal lattice, the more powerful novel multi-channel-detector devices are driven in angular space since this maximizes the yield from any particular setting of the goniometer angles. These detectors were used to build novel X-ray diffractometers, X1 and X2, which will now be described.

(a) *Diffractometers*

(i) *X1*

This diffractometer (figure 5) has the basic four degrees of freedom like any four-circle diffractometer plus the additional advantage of x and y translation of the goniometer cradle and of allowing the detector to be moved for out of plane scattering (Υ) (figure 6). Copper Kα_1 X-rays are produced in a fixed anode generator, passed through a set of collimator slits onto a focussing monochromator and two further sets of slits to the sample. The focal length of the monochromator is 450 mm, and the final slits can be varied between $\frac{1}{20}$ and 3 mm in width and height. All slits are rectangular. The height of the sample has to be carefully adjusted such that the distance to the detector is always 250 mm to avoid a shift in the 2θ position of the Bragg peaks.

PHILOSOPHICAL TRANSACTIONS OF THE ROYAL SOCIETY A
MATHEMATICAL, PHYSICAL & ENGINEERING SCIENCES

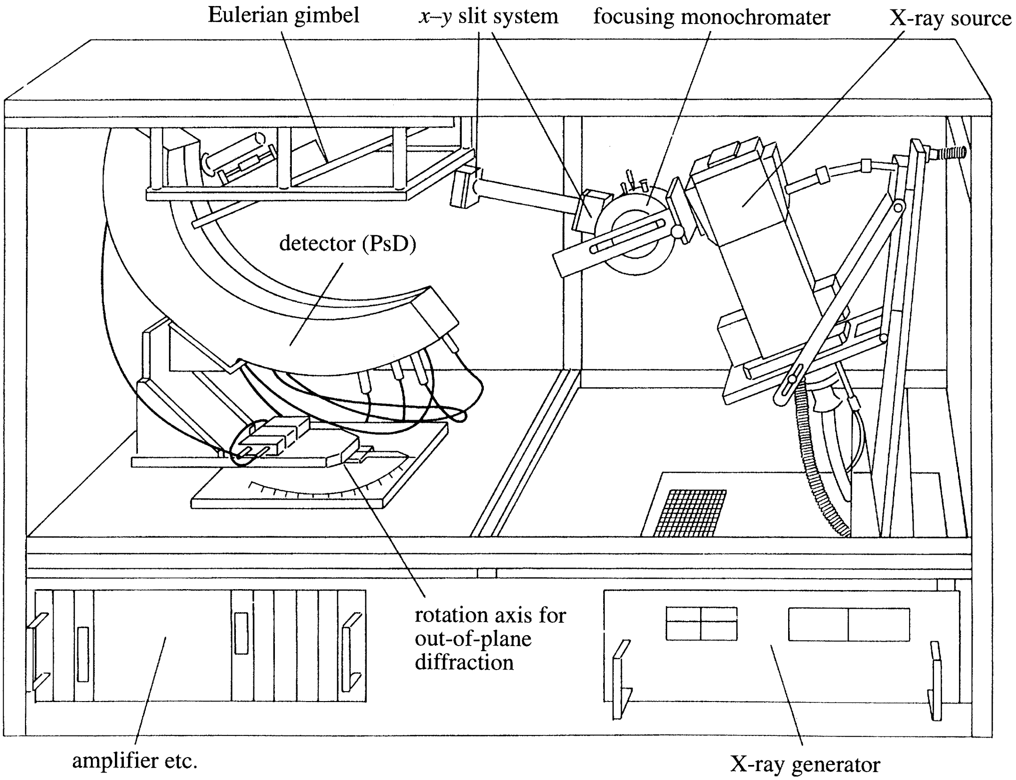

Figure 5. Diagram of the X1 diffractometer.

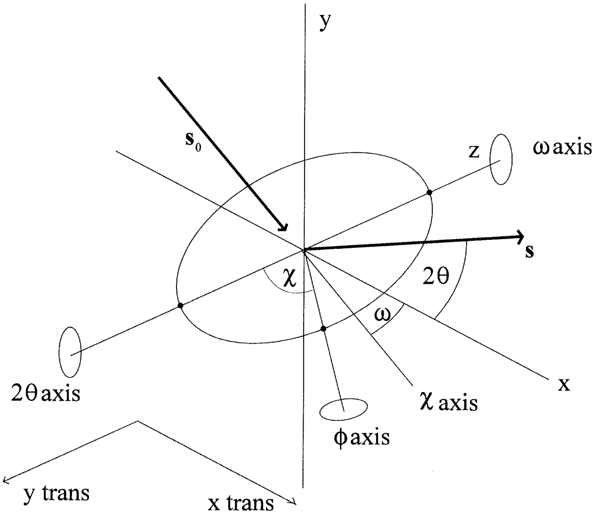

Figure 6. The basic geometry of both the X1 and X2 diffraction systems. The detector can additionally be rotated about the y-axis (ϒ, not in the diagram).

The detector consists of a blade that forms the anode and a delay line constituting the cathode, contained within a gas mixture of argon–ethane under pressure to improve quantum efficiency (INEL). The gas is held at constant pressure within the detector. High voltage is maintained between the two poles to accelerate charges

PHILOSOPHICAL TRANSACTIONS OF THE ROYAL SOCIETY A MATHEMATICAL, PHYSICAL & ENGINEERING SCIENCES

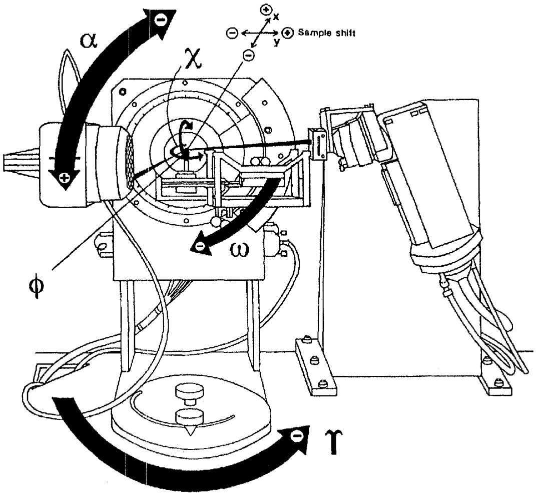

Figure 7. Schematic representation of the basic geometry of the X2 diffractometer system developed at Cambridge

that are freed by interactions of the gas with incoming X-rays. A cascade ensues, and the charges are collected by the cathode. All 4096 sections of the cathode are connected by a delay line that enables the discriminator electronics to determine the exact location of the incident photon by measuring the difference in arrival time between the two ends of the line. The advantages of such a device are obvious, in that the measurements can be performed in real time as opposed to photographic methods, and the whole range of 120°, 2θ is covered simultaneously.

As a result of the latter point no efforts were made to produce software that allows direct scans of reciprocal space such as in conventional four-circle machines with a single channel detector. It proves more efficient to perform experiments using direct angular space and then to convert the collected data to reciprocal space afterwards precisely because a whole array of detectors is given at any one time.

The diffractometer is connected to a 486PC with controlling software that allows the continuous display of the counts in all 4096 channels. The various degrees of freedom are controlled by five stepping motors which can be moved both manually and by software. Programs are installed that allow automated data-collection once the sample has been properly aligned.

(ii) *X2*

The X2 system is similar to X1, with seven degress of freedom (figure 7). The main difference lies in the detector system. Instead of a blade, the X2 detector consists of a multiwire grid enclosed by pressurised xenon gas at approximately 4 bar. The X-rays enter through a concave beryllium window, causing ionization of the gas. The multiwire grid feeds position sensitive decoding circuitry that generates the x–y coordinates of incident photons. The resolution of the 512×512 pixel array can be varied by moving the detector away or towards the sample, with a maximum distance of 300 mm giving an average resolution of 0.028°. Unlike with the X1, the gas is sealed into the detector.

The data collected by the detector are passed on to a PC running a dedicated control and data-analysis program that is part of the X2 package. Incident X-rays are displayed as points on the screen, with the colour indicating the number of counts.

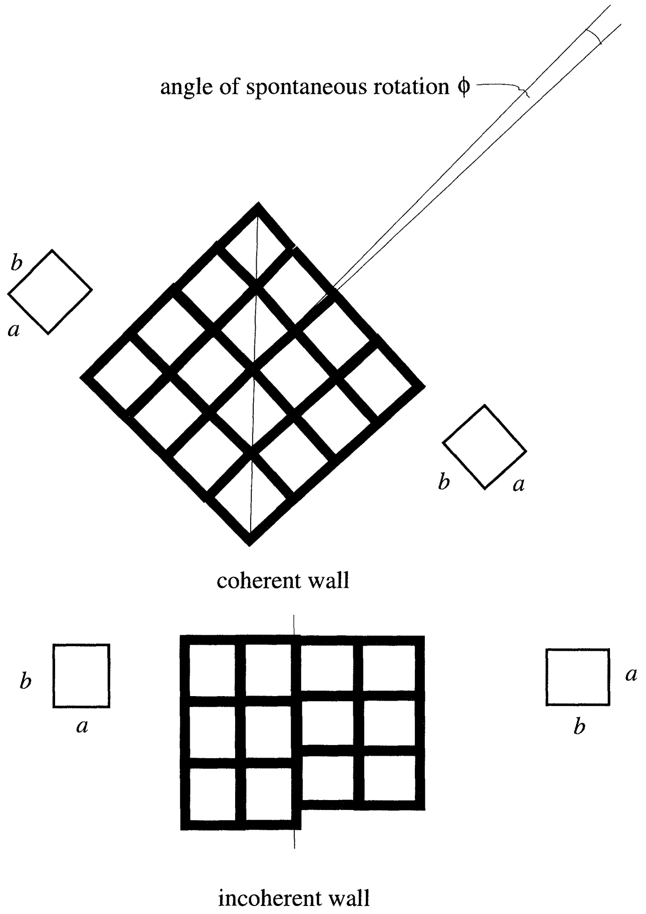

Figure 8. Schematic representation of the strain field caused by the tetragonal to orthorhombic transition in the a–b plane. The walls are along the $\langle 110\rangle$ directions are coherent (above). Walls along $\langle 100\rangle$ directions are also possible (below). However the interface is obviously discontinuous.

Even though frames are saved in an X2 format that minimizes the amount of memory used, the number of pixels of 512 × 512 gives at least 256 kbytes with a maximum of 256 counts per pixel. Any counts in excess of this number are stored in an overflow table that further complicates the file format. It is obvious that the manipulation of these files calls for great computational and memory power. As a result further analysis of the frame files was conducted using a Hewlett-Packard 712/60 workstation (HP) and the Advanced Visual Systems (AVS) graphics package.

(*b*) *Transformation direct → reciprocal space*

A program called 'hkl' was written to enable data from both the X1 and the X2 system to be converted from direct, angular, to reciprocal space. It runs on an HP workstation and converts every single point from the original data file to reciprocal space by applying various rotational matrices to the diffraction vector. The diffraction pattern is then visualized and analysed using AVS.

5. Examples

(*a*) *The transitional regime between twin and tweed structures in* Al-*doped* $YBa_2Cu_3O_{7-\delta}$

Ferroelastic $YBa_2Cu_3O_{7-\delta}$ undergoes a phase transition from space group symmetry $P4/mmm$ in the high temperature phase to $Pmmm$ at 970 K for $\delta \sim 0.15$ (Roth *et al.* 1987; Van Tendeloo *et al.* 1987). The loss of symmetry is caused by the ordering of oxygen atoms in the basal plane of $YBa_2Cu_3O_{7-\delta}$. This transformation is accompanied by the appearance of a spontaneous strain and a spontaneous rotation (Wadhawan 1988; Salje 1990) (figure 8). The strain tensor is given in general by

$$\epsilon_{ik} = \frac{1}{2}\left(\frac{\partial u_i}{\partial x_k} + \frac{\partial u_k}{\partial x_i} + \frac{\partial u_l}{\partial x_i}\frac{\partial u_l}{\partial x_k}\right). \tag{5.1}$$

This can be approximated for the spontaneous strain by

$$e_0 = 2(b-a)/(b+a), \tag{5.2}$$

and the rotation is given by $\phi = 45° - \arctan(b/a)$. Coherent domain walls result in the $\langle 110\rangle$ and $\langle \bar{1}10\rangle$ directions of the lattice. The angle between these domain walls is $90°-2\phi$. However, it is also possible for domain walls to form along $\langle 100\rangle$ directions (figure 8). These are incoherent due to the apparent mismatch between the two domains and dislocations result. Coherent walls are thus favoured as they generally result in a lowering of the Gibbs free energy of the system. The condition for strain compatibility was given by Sapriel (1975) as

$$\det|\epsilon_{ij}^{(1)} - \epsilon_{ij}^{(2)}| = 0, \tag{5.3}$$

$$\operatorname{tr}\left(\epsilon_{ij}^{(1)} - \epsilon_{ij}^{(2)}\right) = 0. \tag{5.4}$$

A strain of type $\epsilon_{xx} - \epsilon_{yy}$ satisfies these conditions (Sapriel 1975; Bratkovsky *et al.* 1994*a*). The strain is linearly proportional to the order parameter (2.7). Hence (2.20) can be used to describe the structure of the domain walls:

$$e = e_0 \tanh(r/w), \tag{5.5}$$

where r is now the distance along $\langle 110\rangle$ and w is the width of the wall.

Experiments were performed on single crystal samples. Details of the crystal growth and thermal treatment have been published elsewhere (Drake *et al.* 1994; Hirst *et al.* 1994). A series of Al-doped samples were used. The samples were heated to 800 °C in pure oxygen. They were then cooled to room temperature at 5 °C h^{-1} and subsequently annealed under flowing oxygen at 450° for 10 days.

To get the best results it was decided to choose the (200)/(020) peak group with its large scattering amplitude and orthorhombic splitting. For this the *a*-axis geometry had to be employed, as depicted in figure 9.

A consequence of the appearance of a spontaneous strain in $YBa_2Cu_3O_{7-\delta}$ is that reflections with at least one non-zero index are split four-fold. It can be shown (Steinborn *et al.* 1994) that for $(h0l)$ reflections the positions of the peaks are described by

$$\left(\left\{\begin{matrix} a \\ a \\ b \\ b \end{matrix}\right\} \frac{\sqrt{2}}{\sqrt{a^2+b^2}}\,h, \left\{\begin{matrix} a \\ -a \\ b \\ -b \end{matrix}\right\} \frac{(b-a)}{(b+a)}\frac{\sqrt{2}}{\sqrt{a^2+b^2}}\,h, l\right). \tag{5.6}$$

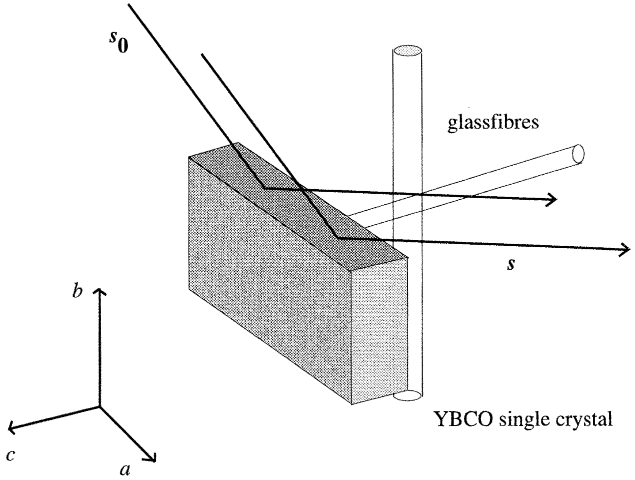

Figure 9. The a-axis geometry for single crystals. A glass fibre is glued vertically into a screw mounted on the goniometerhead. In contrast to thin films for single crystals a second, transverse, fibre is added to the first, with the sample glued onto its end such that the a–b axis is in the diffraction plane.

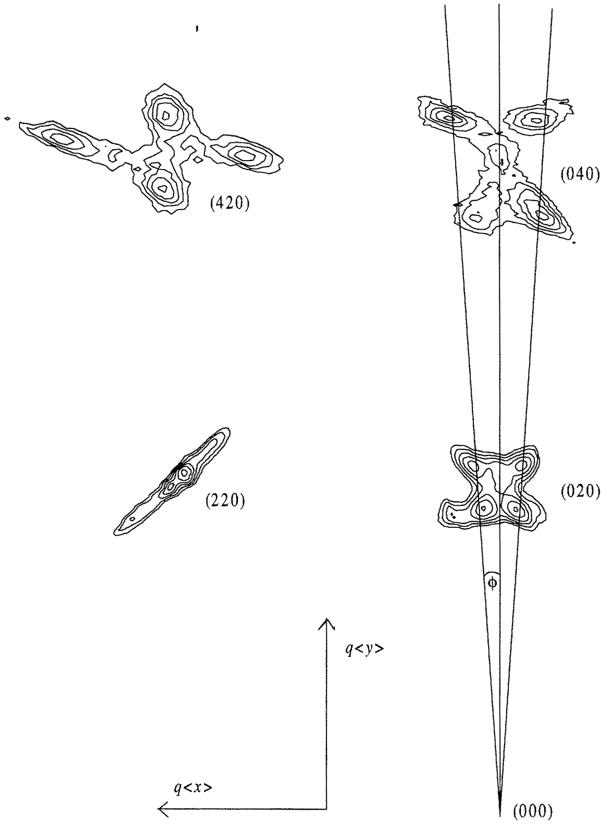

Figure 10. Mapping of reciprocal space for a single crystal doped with $x = 0.01$. ϕ is the angle of spontaneous rotation. Distances and angles are not to scale.

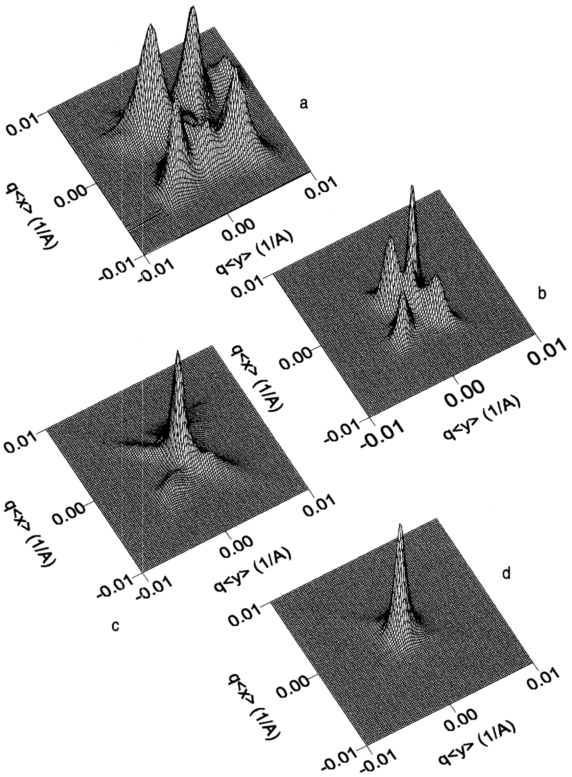

Figure 11. Surface plots of the Al-doped $YBa_2(Cu_{1-x}M_x)_3O_{7-\delta}$ single crystal series in reciprocal space: (*a*) $x = 0.01$; (*b*) $x = 0.02$; (*c*) $x = 0.03$; (*d*) $x = 0.04$. Notice the orthorhombic to tetragonal phase transition.

The Miller indices here refer to the average, tetragonal, lattice constants $\frac{1}{2}(a+b)$. For the case $b - a \ll \frac{1}{2}(a+b)$ this reduces to (Kromann *et al.* 1992)

$$((1 \pm \tfrac{1}{2}e_0)h, \pm\tfrac{1}{2}e_0 h, l). \tag{5.7}$$

In terms of reciprocal coordinates, the spontaneous strain is thus given by

$$e_0 = \left(\left\{ \begin{matrix} a \\ -a \\ b \\ -b \end{matrix} \right\} \frac{\sqrt{2}}{\sqrt{a^2+b^2}}\, h \right)^{-1} (a+b)\delta q_y, \tag{5.8}$$

$$e_0 \sim \frac{(a+b)}{h}\delta q_y. \tag{5.9}$$

An illustration of several reciprocal lattice points and their relation to one another is given in figure 10. The angle of spontaneous rotation is exaggerated and the scaling incorrect.

With increasing Al content one observes a transition to the high-temperature phase

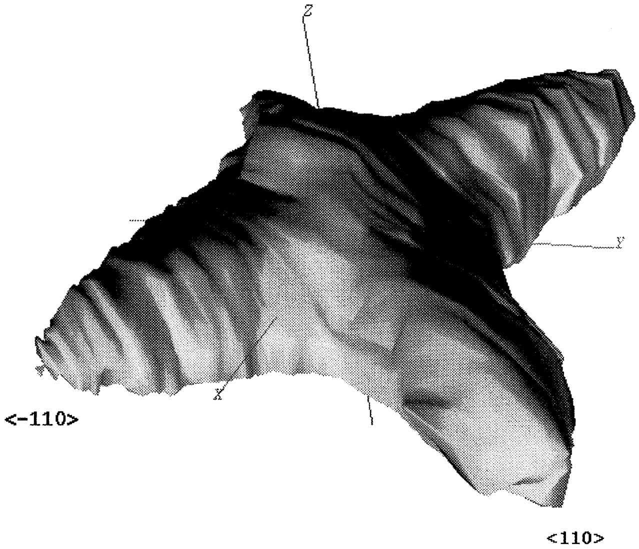

Figure 12. An isosurface representation of the (200)/(020) reflection for a single crystal doped with $x = 0.04$ aluminium. The value of equal intensity is about a hundredth of the maximum at the centre. Axis range is $(-0.006, -0.006, -0.006)$–$(0.006, 0.006, 0.006)$ in Å^{-1}.

at between $x = 0.02$ and 0.03 (figure 11), as was also found by (Drake *et al.* 1994; Hirst *et al.* 1994). This agrees with the discussion in § 2. Changing the concentration of impurities is equivalent to changing the transition temperature of the crystal. Strong streaking along the ⟨110⟩ directions indicates diffuse scattering from domain walls. At nominal $x = 0.02$ Al in $YBa_2(Cu_{1-x}M_x)_3O_{7-\delta}$ a tetragonal peak appears, a sign that both tweed and twins coexist, most likely in different regions of the crystal (Hirst *et al.* 1996). The diffuse streaks vanish nearly completely at $x = 0.04$, an indication that the sample is now essentially disordered and overall tetragonal.

(*b*) *Tweed in* Al-*doped* $YBa_2Cu_3O_{7-\delta}$

A single crystal of $YBa_2(Cu_{1-x}M_x)_3O_{7-\delta}$ with nominally $x = 0.04$ Al content was chosen to be investigated. The result of scanning reciprocal space around the peak group (200)/(020) is shown in figure 12. The diffraction pattern is known as a ‘butterfly’. The most important features are the streaks along the ⟨110⟩ directions.

Lines of intensity versus distance were extracted from the three-dimensional structure using AVS. The three major crystallographic directions and their intensity are plotted in figure 13 as a superposition on a log–log scale. A reduced wavevector ξ gives a dimensionless measure along various directions in the crystal. It is immediately noticeable that the ⟨110⟩ directions are distinctly different from the other directions. The peak is analysed using three components:

(i) the Bragg peak for small values of $\xi < 3 \times 10^{-3}$;

(ii) an intermediate region $3 \times 10^{-3} < \xi < 6 \times 10^{-3}$ that seems to follow a $1/k^2$ dependence; and

(iii) an outer region $\xi > 6 \times 10^{-3}$ that observes a $1/k^4$ dependence of the diffracted intensity.

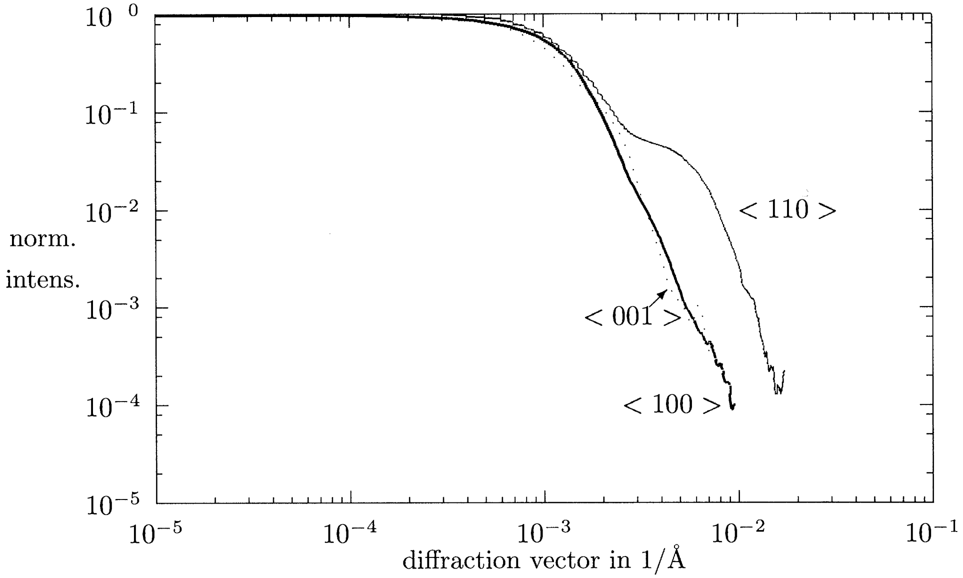

Figure 13. Log–log plot of intensity versus wavevector for various directions for the $x = 0.04$ sample. The diffuse scattering in the $\langle 110\rangle$ direction is clearly visible.

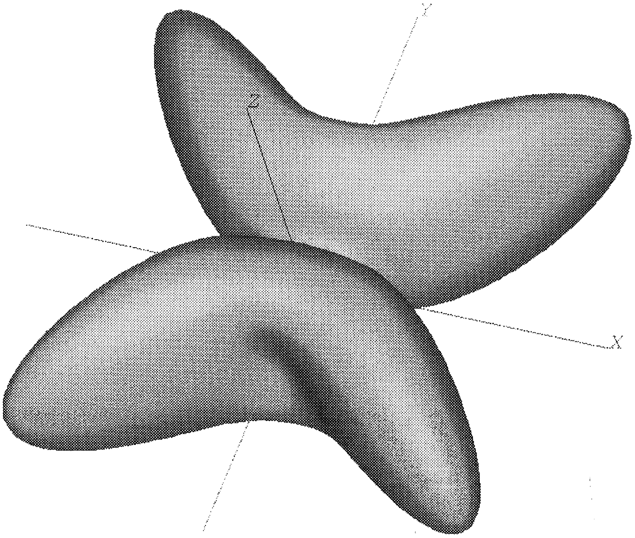

Figure 14. Isosurface plot of the diffuse scattering generated by calculating the static displacements in $YBa_2Cu_3O_{7-\delta}$.

According to many theoretical predictions intensity should indeed be a function of $1/k^2$ for small k and $1/k^4$ for large k. Such a behaviour would correspond to straight lines in a log–log plot of slope -2 and -4. It is evident that even though the $1/k^2$ dependence is pronounced in the $\langle 110\rangle$ directions, this is not so for the $\langle 100\rangle$ and $\langle 001\rangle$ direction. In the latter the drop off leads rapidly into what is closer to $1/k^4$.

A characteristic lengthscale is defined by the crossover between the $1/k^2$ and $1/k^4$

behaviours for the ⟨110⟩ direction and gives a value in the range of 130 → 170 Å. Considering the difficulties in extracting and estimating the length scales the agreement with Schmahl *et al.* (1989) and Jiang *et al.* (1991, 1992) is reasonable. The former found a twin spacing of between 40–60 Å just beyond the orthorhombic to tetragonal transition, which corresponds to wavelengths of 80–120 Å—roughly what is observed here.

An isosurface plot of the calculated diffraction pattern obtained using the static displacement wave approach and thermal diffuse scattering is shown in figure 14. The thermal diffuse scattering proves negligible in comparison to the critical scattering along the ⟨110⟩ directions, which is why it does not show up. The essentials are reproduced, in all three directions, if one imagines the Bragg peak filling the centre (the algorithm calculates the diffuse scattering only).

(*c*) *Determination of twin wall thickness in* $YBa_2Cu_3O_{7-\delta}$ *single crystals*

Large single crystals of $YBa_2Cu_3O_{7-\delta}$ ($2 \times 2 \times 0.2\ \mathrm{mm}^3$) were chosen from three different crystal-growth experiments and were shown to have a sharp (1K) transistion at $T_c \approx 92$ K. Domains were visible under crossed polarizers. Rocking experiments were performed on the (029)/(209), (02.10)/(20.10) and (02.11)/(20.11) peaks to get maximum orthorhombic splitting in the *c*-axis configuration. The domain wall profile given in (5.5) was used to analyse the diffraction pattern (Chrosch & Salje 1994).

To calculate the displacement pattern caused by the strain field we integrate

$$\delta y = \int e\,\mathrm{d}r \tag{5.10}$$

$$= C \ln(\cosh(x/w\sqrt{2})). \tag{5.11}$$

The intensity is proportional to the square of the structure factor given by

$$F = \sum \cos[2\pi(hx + ky)] + \mathrm{i} \sum \sin[2\pi(hx + ky)]. \tag{5.12}$$

A linear model with the variable x being an integer in the range of $-2N \cdots 2N$ and y given by

$$y(x) = \begin{cases} Cw \ln\cosh(x/w\sqrt{2}), & \text{if } -N \leqslant x \leqslant N, \\ 2y(N) - y(2N - x), & \text{if } -2N \leqslant x < N, \text{ and } N \leqslant x < 2N, \end{cases} \tag{5.13}$$

describes two domains for $x > 0$ and $x < 0$, respectively, and domain walls of thickness w at $x = 0$ and $x = \pm N$.

The intensity ratio $I_{\mathrm{w,tot}}$ of wall intensity and total intensity can be calculated as

$$I_{\mathrm{w,tot}} = \frac{I_{\mathrm{wall}}}{I_{\mathrm{total}}} \tag{5.14}$$

$$= \frac{f(w)}{2ds}, \tag{5.15}$$

where $f(w)$ is the wall-related intensity function and $s = 0.5°/kC$ a scaling factor between experiment and calculation. From this w and d can be extracted.

A wall thickness of $w \approx (7 \pm 2)$ Å was found at room temperature (Chrosch & Salje 1994). Under the assumption that the whole crystal is twinned this gives an average domain size of $d \approx 230$ Å. This was confirmed by HRTEM measurements yielding $d \approx 200$ Å.

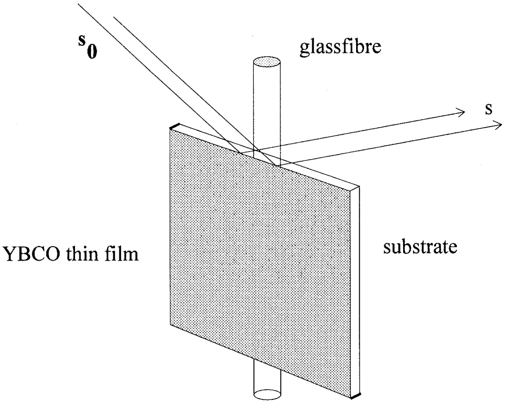

Figure 15. The a-axis geometry for thin films. The substrate is glued directly onto the fibre. For the c-axis geometry in thin film experiments the sample is attached straight onto the goniometerhead using double-sided tape.

Using $T_c \approx 1020$ K and $T = 300$ K we find $gT_c/A \approx a^2$, where a is the lattice parameter perpendicular to the wall (i.e. 5.5 Å). This is identical to the Ginzburg conjecture $gT_c/A = a^2$, enabl ing an estimate of the Ginzburg parameter g to be made. Assuming an entropic prefactor of $A \approx 40\ \mathrm{J\ mol^{-1}}$ leads to $g \approx 1 \times 10^{-20}\ \mathrm{J\ m^2\ mol^{-1}\ K^{-1}}$.

(*d*) Al-*doped* $YBa_2(Cu_{1-x}M_x)_3O_{7-\delta}$ *films*

X-ray diffraction experiments were performed on five samples of varying Al content, from nominal $x = 0$ to 0.1 (Yeadon *et al.* 1995; Yeadon *et al.* 1996). The samples were grown and supplied by F. Wellhöfer (as cited in Yeadon *et al.* 1993; Aindow *et al.* 1994) of the University of Birmingham.

Data on the growth of the films was provided by F. Wellhöfer. Films were grown on MgO single crystal substrates of dimensions $5 \times 5\ \mathrm{mm^2}$ with polished (100) faces using laser ablation techniques. Ablation took place at 780 °C in 400 mTorr oxygen atmosphere for 30 min. The heater was then switched off and the ablation chamber backfilled with oxygen to *ca.* 700 mTorr. The samples were subsequently cooled down to room temperature within about two hours. The films are orientated such that the c-axis is orthogonal to the substrate and the a- and b-axes are parallel to the substrates edges.

No distinct domain structure was found using optical microscopy with crossed polarizers (Yeadon *et al.* 1995, 1996). For conducting diffraction experiments two geometries were employed to be able to access relevant peaks. The samples were mounted onto specimen holders with double-sided tape for the c-axis geometry and onto glass fibres, as indicated in figure 15, for the a-axis geometry. First, rocking experiments for the c-axis geometry were performed for the family of peaks (007), (10.10) and (20.11). However, the relative orthorhombic split in the latter two is not large enough to be resolved for the doped samples (see figure 16). Table 1 gives the splitting for several peaks as predicted by assuming lattice parameters of $a = 3.8206$ Å, $b = 3.8851$ Å and $c = 11.6757$ Å (Capponi *et al.* 1987).

It can be easily seen from table 1 that splitting becomes very difficult to resolve when one takes into account the intrinsic peak broadening in thin films. Typically the FWHM for the individual peaks is 0.6° in 2θ, which can just about be resolved according to table 1. It was thus concluded that the a-axis configuration was more

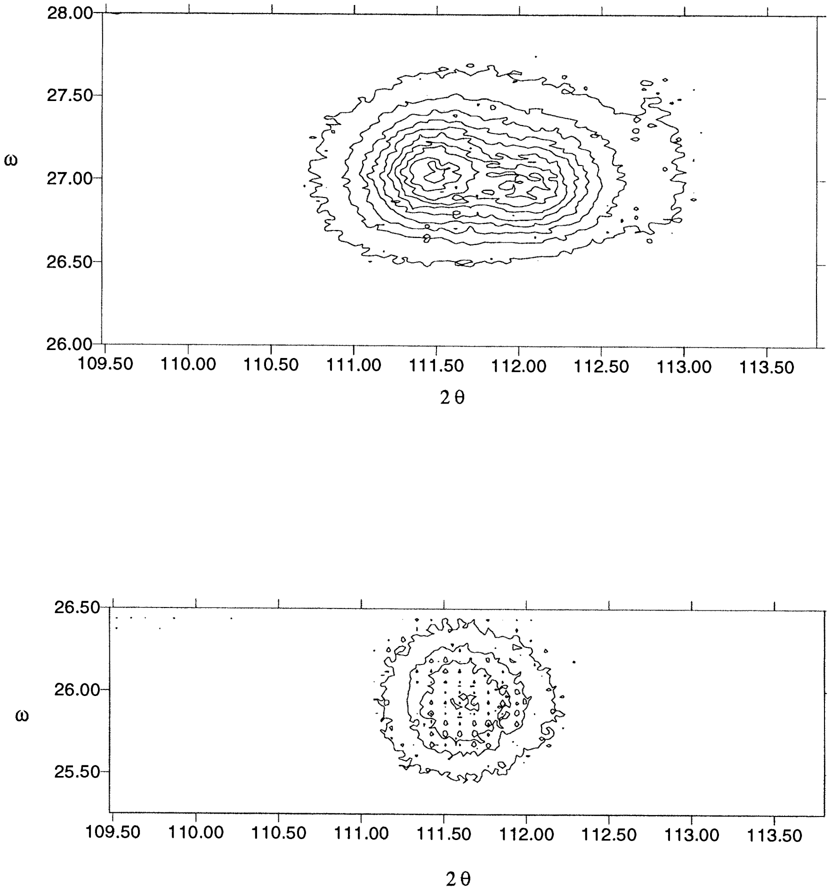

Figure 16. The (20.11)/(02.11) peak group in $YBa_2Cu_3O_{7-\delta}$ thin films doped with (*a*) $x = 0$ and (*b*) $x = 0.012$ Al. ω is the angle of incidence of the X-ray beam with respect to (001). No split in the 0.012 sample is apparent (this sample was not included in the later analysis since it had only half the thickness of the other specimens in the series).

promising, although this meant that diffraction would have to take place *off the edge of the film*, which obviously results in very low intensities. This, however, is partly offset by the fact that the (200/020) peak group has a very large structure amplitude and is thus intrinsically very intense. Also, full automation of diffraction experiments allowed for long counting periods with data collection taking typically 24 h. The *a*-axis experiments were performed exclusively on the X2 system, since small misalignments of the sample in χ do not necessarily result in the disappearance of a given reflection as would be the case on a one-dimensional detector but simply

Table 1. *Angle* ψ *between (hkl) and (001) (above) and (hkl) and (100) (below), angle of incidence* ω*, angle of diffraction* 2θ *and peak split for various (hkl) values in* $YBa_2Cu_3O_{7-\delta}$ *for* $\delta \sim 0.15$.

h	k	l	ψ	ω	2θ	split in ω in 2θ
1	0	7	23.580	6.670	60.520	0.270
0	1	7	23.230	6.940	60.340	0.180
1	0	8	20.910	13.490	68.800	0.240
0	1	8	20.590	13.730	68.640	0.160
1	0	9	18.771	20.046	77.633	0.217
0	1	9	18.474	20.263	77.472	0.161
1	0	10	16.993	26.626	87.238	0.194
0	1	10	16.723	26.820	87.085	0.153
2	0	9	34.205	11.653	91.716	0.140
0	2	9	33.750	11.793	91.086	0.630
2	0	11	29.058	27.063	112.242	0.075
0	2	11	28.653	27.138	111.581	0.661
2	0	0	0	23.780	47.560	0.420
0	2	0	0	23.360	46.720	0.840
4	0	0	0	53.750	107.500	1.275
0	4	0	0	52.475	104.950	2.550

of a given reflection as would be the case on a one-dimensional detector but simply move it along a conic of constant 2θ. Counting times of typically 400 s per frame were employed, over a range of 3–4° in ω in steps of 0.02°. Once the data had been collected we integrated the intensities along conics of constant 2θ in χ to calculate the integrated intensity for every ω and assemble the series of frames into one single file containing ω, 2θ and *intensity*. This in turn was converted to reciprocal space, the result of which is figure 17. The lattice constants for the conversion were taken as $a = b = 3.85285$ Å and $c = 11.6757$ Å (cf. § 5 *a*).

The peaks were then fitted for slices through the maximum intensity to get the splitting, given by (5.2)

$$e_0 = \frac{\Delta q_y (a+b)}{2h} \quad (\text{see § } 5\,a). \tag{5.16}$$

The resulting variation is shown in figure 18. Plotting ϵ^2 versus concentration clearly shows a linear relationship, with a transition to tetragonal at $x = 0.056$. Notice the plateau effect in figure 18 mentioned in § 2. The error in the value at $x = 0.05$ is large since it was difficult to distinguish the split peaks by inspection because they were so close.

Peak fitting failed to give the separation for the $x = 0.05$ sample, so it was estimated from the line profile in reciprocal space. To make sure that the nominal Al content is *de facto*, electron microprobe experiments were conducted. The result is

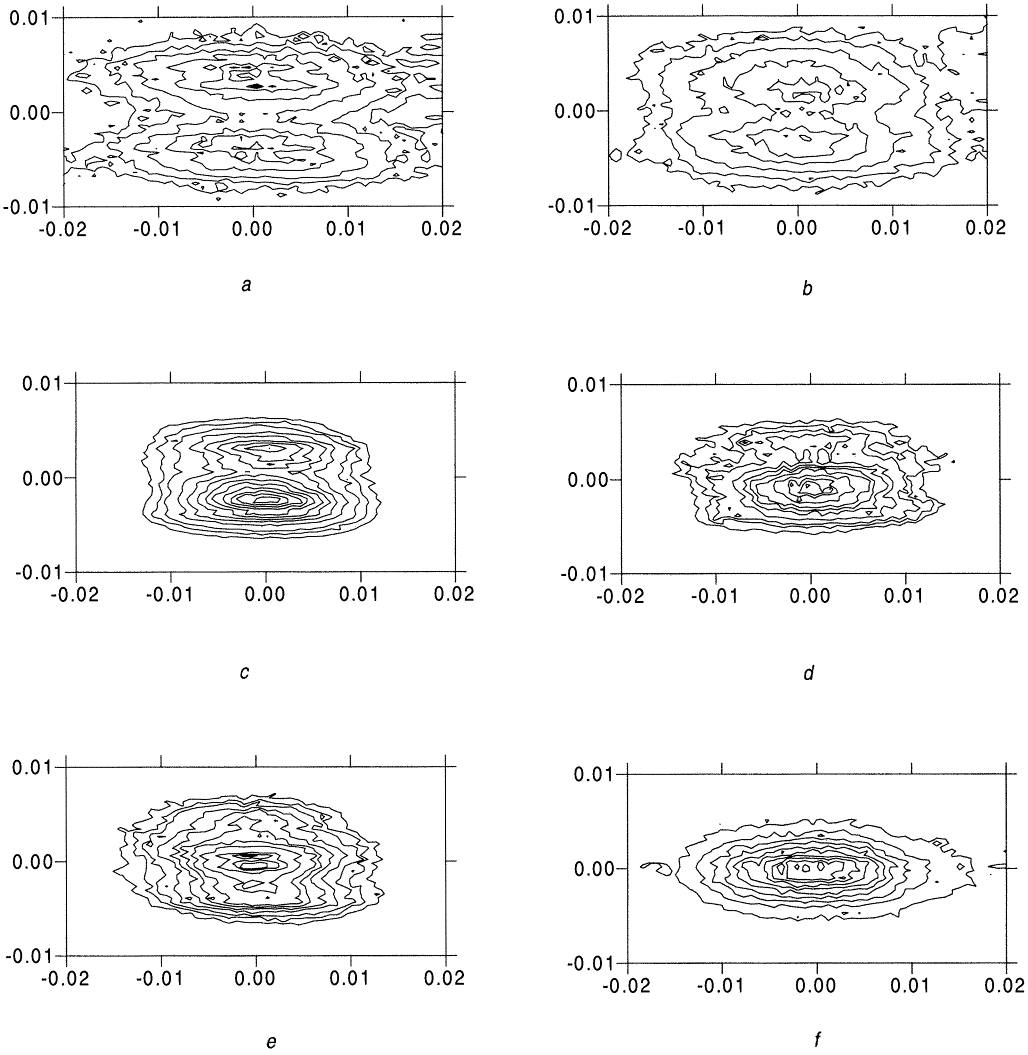

Figure 17. The development of the (200)/(020) peak group in an $YBa_2Cu_3O_{7-\delta}$ thin film as a function of Al content: (*a*) $x = 0$; (*b*) $x = 0.02$; (*c*) $x = 0.03$; (*d*) $x = 0.04$; (*e*) $x = 0.05$; (*f*) $x = 0.1$. The contour plots show intensity in the k_x–k_y plane. Units are Å^{-1}. The transition takes place between 0.05 and 0.1, even though the split in (*e*) is hardly visible (see text).

shown in figure 19. The agreement is excellent. The data were extracted from the ‘raw data’ by using dedicated software for thin film analysis. It also returned a value for the film thickness which is on average 0.5 μm.

The result of these measurements is in contrast to what is found in bulk

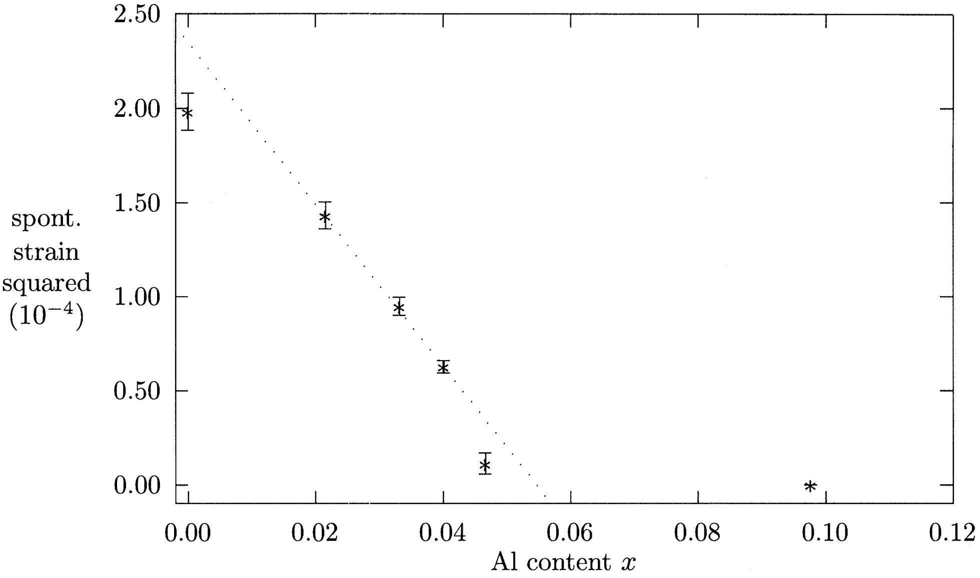

Figure 18. Strain as a function of Al concentration in $YBa_2Cu_3O_{7-\delta}$ thin films. The line is a guide for the eye and indicates a power-law behaviour predicted by a classical 2nd order phase transition due to bi-linear coupling of the order parameter to strain.

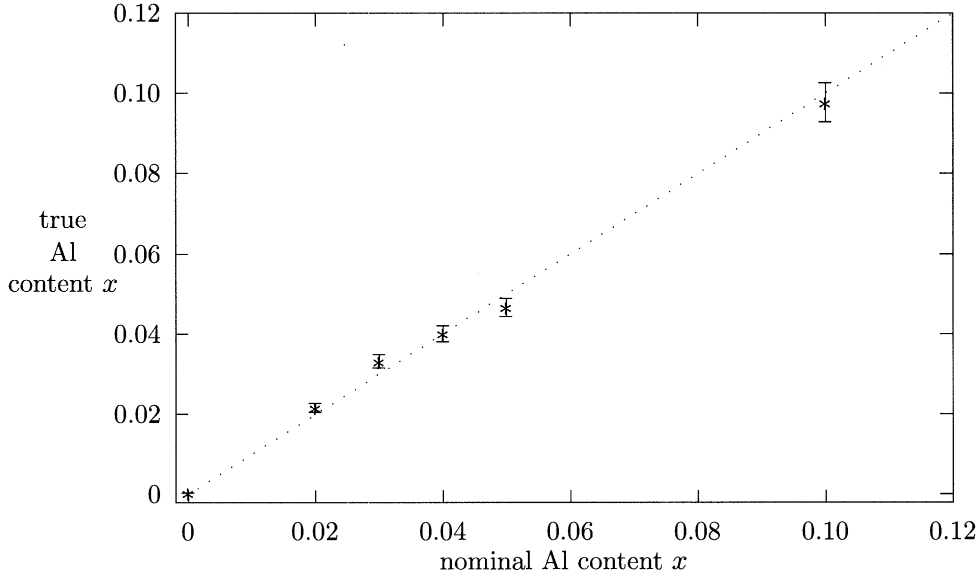

Figure 19. Plot of real versus nominal Al content x in the investigated $YBa_2Cu_3O_{7-\delta}$ thin films as obtained from electron microprobe analysis. The line is a guide for the for the eye and indicates a 1:1 correspondence.

$YBa_2(Cu_{1-x}M_x)_3O_{7-\delta}$, where the critical concentration of Al has been found to be of the order of $x = 0.03$ (Hirst *et al.* 1994; Lacayo *et al.* 1992). It thus seems that the orthorhombic phase is stabilized. There are several major differences between thin films and bulk:

(i) the film is essentially two dimensional;

(ii) there is a lattice mismatch between film and substrate, causing a strain profile in the ⟨001⟩ direction; and

(iii) oxygen and Al diffusion lengths are longer in thin films.

The most important point is the second. It has been found that undoped films grown on $SrTiO_3$, the lattice constants of which match $YBa_2Cu_3O_{7-\delta}$ much better than MgO, show a much smaller spread in the orientational distribution of the *a*- and *b*-axis in the (001) plane (mosaicity) (Kromann *et al.* 1992). Unfortunately such an experiment could not yet be made by the authors since no full Al-doped series on $SrTiO_3$ has been available to date. The two films at $x = 0$ and 0.05 that could have been used were in fact difficult to measure since there is a strong substrate peak only *ca.* 0.2° below the $YBa_2Cu_3O_{7-\delta}$ peak in 2θ. This is a large obstacle to using the *a*-axis geometry, and other methods will have to be found to measure the splitting of thin films on $SrTiO_3$ substrates.

Mosaicity is the reason why only two of the four orthorhombic peaks are resolved in diffraction experiments. The variation of the *a*–*b*-plane mosaicity has been determined in figure 20 using the following method. The diffraction profile for the films was fitted using Gaussian line-shapes to determine the FWHM in ω. It was then assumed that instrumental broadening can safely be described by a Gaussian, as was verified by using a silicon standard. The intrinsic FWHM of the spread in *a*–*b* should thus be given by (Kromann *et al.* 1992)

$$\omega^2_{\text{peak}} = \omega^2_{\text{spread}} - \omega^2_{\text{instrumental}}. \tag{5.17}$$

This follows from the fact that the convolution of two Gaussians is again a Gaussian with the half-widths related as above. It is then ascertained that the intrinsic spontaneous rotation within the *a*–*b* plane is given by

$$\phi = 45° - \arctan\left(\frac{2+\epsilon}{2-\epsilon}\right). \tag{5.18}$$

Twice the value of ϕ is then substracted from ω_{spread} to get the intrinsic variation of the *a*–*b*-plane orientation. It seems that the mosaicity increases with increasing aluminium content. This can be accounted for by assuming that the addition of impurities increases disorder in the sample, but also it signifies the disorder intrinsic to tweed and the fact that the microdomains do not align perfectly along ⟨110⟩ directions, as one would expect. It thus seems reasonable to assume that the film aligns such that the lattice misfit is reduced to a minimum. In the tetragonal phase the accommodation of the lattice misfit is facilitated by the reduction in size of the single domain units, if a microdomain model is assumed, producing a larger variation in the (001) plane axes alignment.

In figure 21 the grain size of the thin films is displayed, as determined using the Scherrer formula. It is found that on average the grains are 200 Å, in accordance with Kromann *et al.* (1992). The physical origin of this is likely to be growth features within the film (Yeadon *et al.* 1995).

(*e*) *Determination of the thickness of pericline twin walls in anorthoclase*

Twinning in anorthoclase is a result of the displacive $C2/m \rightarrow C\bar{1}$ phase transition caused by the collapse of the aluminosilicate framework (Brown & Parsons 1994). Symmetry considerations indicate that two twin laws are possible. Albite twins are related by a (010) mirror plane, and so the twins are parallel to (010). Pericline twins are related by a [010] diad, and so the twin plane is $(h0l)$, where the exact values of h

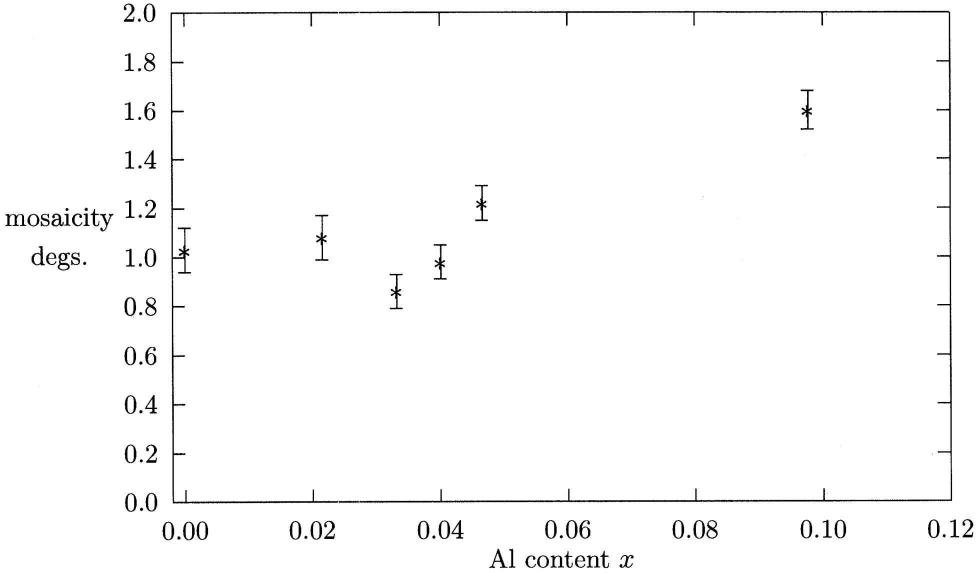

Figure 20. The mosaicity as a function of Al doping x for $YBa_2Cu_3O_{7-\delta}$ thin films on MgO. The disorder in the a-b plane orientation might increase with increasing Al content.

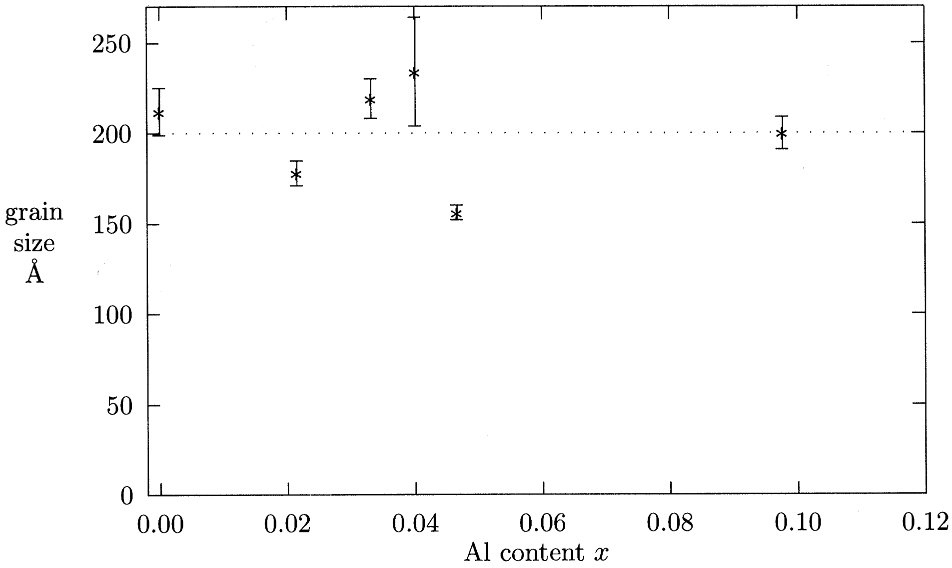

Figure 21. The grain size as a function of Al doping for $YBa_2Cu_3O_{7-\delta}$ thin films on MgO. An average value of 200Å is observed. (Line is guide for eye only.)

and l vary with the lattice parameters, and therefore with thermodynamic conditions. In anorthoclase, this composition plane is approximately (001) (Smith 1974).

The sample used was from volcanic tuffs in Camperdown, Victoria (sample 195127 in the Harker Collection, Cambridge University). Microprobe analysis indicated that its composition was $Na_{0.65}K_{0.30}Ca_{0.05}Al_{1.05}Si_{2.95}O_8$, i.e. $Ab_{65}Or_{30}An_5$.

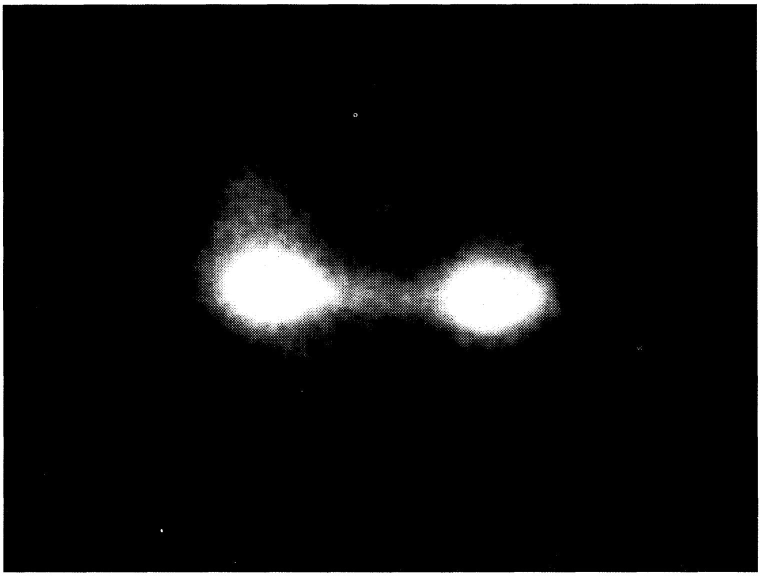

Figure 22. Electron diffraction pattern showing twin-related diffraction peaks in anorthoclase and diffuse streaks due to walls in between.

Table 2. *Peak splitting and intensity ratios as a function of temperature*

temp/K	$\Delta 2\theta$/deg	$I_{\text{wall}}/I_{\text{bulk}}$
295	1.31	0.0170
375	1.18	0.0193
475	0.99	0.0216
525	0.88	0.0229
575	0.83	0.0211
625	0.64	0.0267
675	0.62	0.0321

(010) cleavage slices (typically 3 mm × 3 mm × 0.5 mm) were cut, and the presence of pericline twins was checked optically.

In this experiment, we examined the streaking of pairs of twin-related Bragg peaks. These streaks are the diffraction caused by the twin wall, which can be regarded as a continuous transition between two domains. This streaking can easily be seen in electron diffraction patterns (figure 22), but their extreme weakness makes it impractical to study them using standard X-ray methods.

The form of the raw diffraction data is shown if figure 23. The relevant part of the signal is the streak between the two peaks, and an intensity profile was extracted along this line. The streaking along lines of constant 2θ is related to other modulations in the structure.

The diffracted intensity consists of:

(i) background (which can be estimated from I outside the peaks);
(ii) Bragg peaks; and
(iii) the wall related signal.

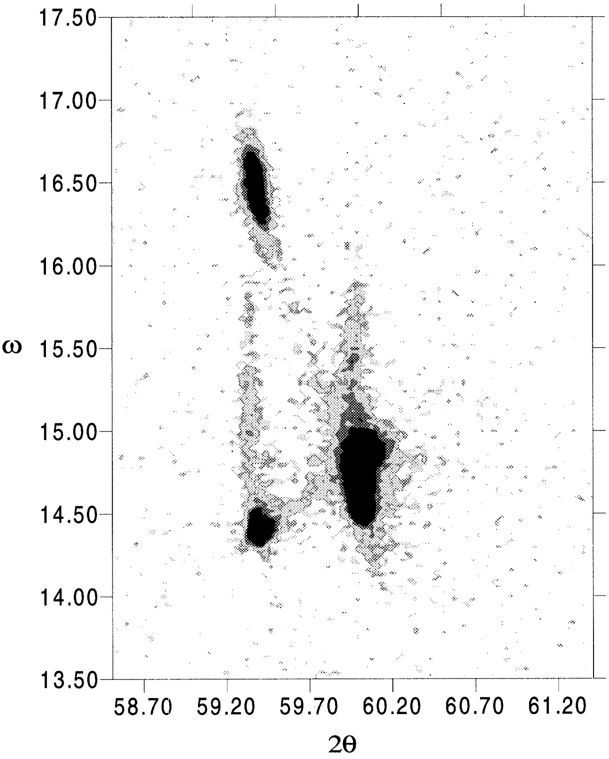

Figure 23. Plot of intensity versus 2θ and ω of experimental diffraction data for anorthoclase sample at 623 K. ω is the angle of incidence between the X-ray beam and (010).

Using figure 23 as a guide, it is possible to estimate the extent of the Bragg peaks, and therefore distinguish between Bragg and diffuse diffraction. From this, an estimate of the fraction of the crystal distorted by twin walls can be made.

To a very good approximation,

$$\frac{V_{\text{wall}}}{V_{\text{bulk}}} = \lambda \frac{I_{\text{wall}}}{I_{\text{bulk}}}, \tag{5.19}$$

where $\lambda \approx 1$.

Furthermore, given an estimate of the spacing between twins, the volume ratios can be used to determine the thickness of the walls—$2w$ in (2.20).

Diffraction patterns were collected at a range of temperatures between room temperature and 725 K. At higher temperatures, the Bragg peaks studied ((081) and $(0\bar{8}1)$) began to overlap significantly. The integrated intensities are listed in table 2.

Electron micrographs (such as those in figure 24) were used to estimate the twin density. Two features of these twins are significant:

(i) The density is not perfectly uniform. Neglecting those areas of the sample that had no pericline twins (probably due to the presence of albite twinning), there was still at least a factor of two variation in the twin spacing across the samples examined.

(ii) The twin structure does not change on heating, and even after annealing above T_c, twins reappear on cooling in the same locations as before. This is presumably due to defects congregating along the twin boundaries.

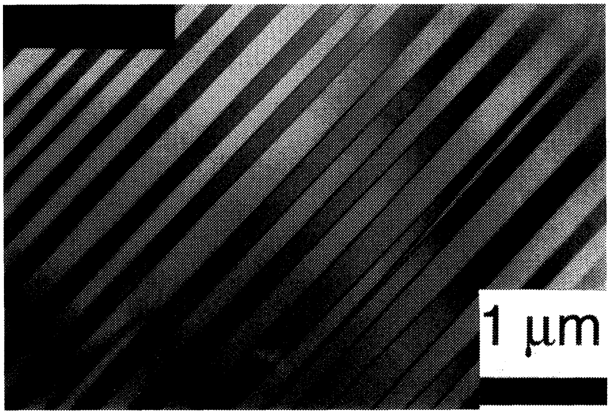

Figure 24. One of the electron micrographs used to estimate twin density in anorthoclase.

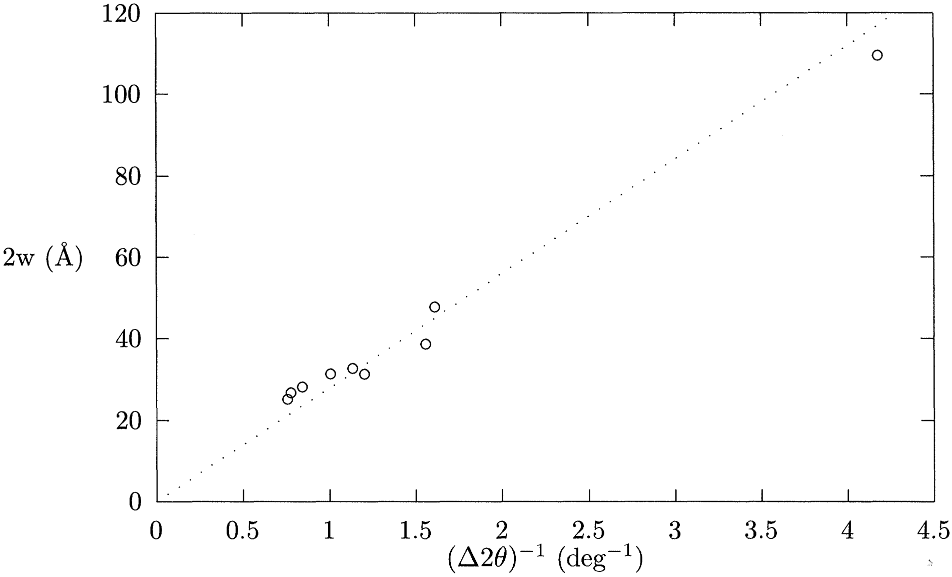

Figure 25. Wall thickness as a function of Q; the large interval between $1/Q = 2$ and $1/Q = 4$ is a result of the rapid variation in Q as T_c is approached.

Given these limitations, an estimate of the spacing of twins is $d \approx (1500 \pm 100)$ Å. The thickness of the walls at room temperature is 1.7% of this (table 2), which is equivalent to a wall width of $2w = (25 \pm 2)$ Å or $w = (13 \pm 1)$ Å.

The variation of wall thickness with temperature was predicted in (2.21). This Ginzburg–Landau model can be tested by plotting the variation of w with Q or with temperature. The resulting relationships are shown in figures 25 and 26.

6. Future work

In this review it was demonstrated how X-ray diffraction can be used to investigate mesoscopic structures in various materials in a routine manner. Future work will extend the above discussed measurement regime to cover low temperatures at one end and even higher detector resolution at the other.

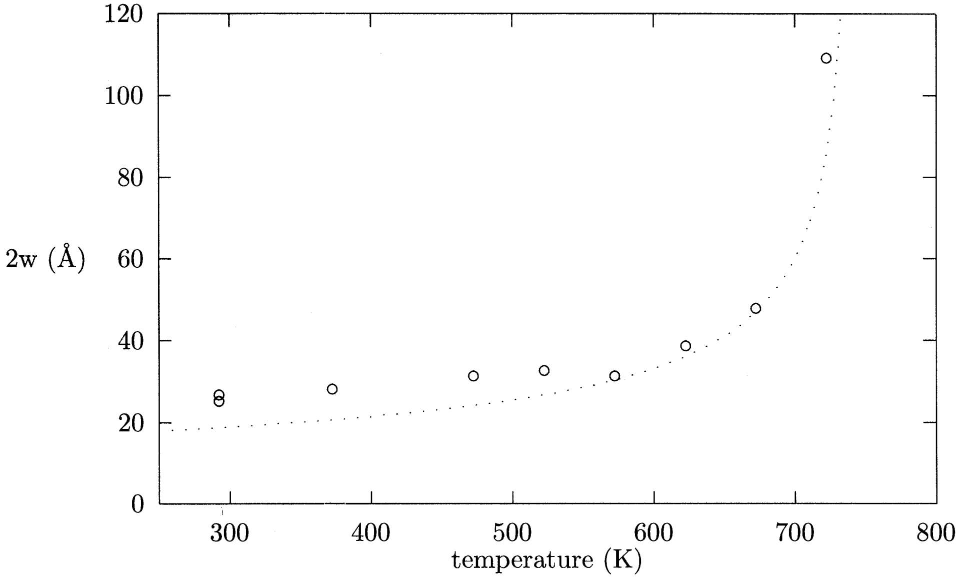

Figure 26. Wall thickness as a function of temperature. The best fit line is constrained to be a purely quadratic function.

The authors thank F. Wellhöfer and P. Woodall, School of Metallurgy and Materials, The University of Birmingham, Birmingham B15 2TT, UK for the provision of $YBa_2(Cu_{1-x}M_x)_3O_{7-\delta}$ thin film samples. The authors also thank A. Buckley for assistance in various aspects of computing, Dr S. Reed for conducting the microprobe analysis and M. Carpenter for help with the TEM, all members of the Department of Earth Sciences, Cambridge.

K.R.L. thanks Magdalene College, Cambridge, for enabling him to continue his work, and S.A.H. thanks the NERC for financial support.

References

Aindow, M. & Yeadon, M. 1994 The origins of growth spirals on laser-ablated $YBa_2Cu_3O_{7-\delta}$ thin-films. *Phil. Mag. Lett.* **70**, 47–53.

AVS 1992 *Developer's guide and application's guide.* Waltham, MA: Advanced Visual Systems Inc.

Bratkovsky, A. M., Salje, E. K. H. & Heine, V. 1994*a* Overview of the origin of tweed texture. *Phase Transitions* **52**, 77–83.

Bratkovsky, A. M., Salje, E. K. H., Marais, S. C. & Heine, V. 1994*b* Theory and computer simulation of tweed texture. *Phase Transitions* **48**, 1–13.

Bratkovsky, A. M., Marais, S. C., Heine, V. & Salje, E. K. H. 1994*c* The theory of fluctuations and texture embryos in structural phase transitions mediated by strain. *J. Phys.* C **6**, 3679–3696.

Bratkovsky, A. M., Salje, E. K. H., Marais, S. C. & Heine, V. 1995 Strain coupling as the dominant interaction in structural phase transitions. *Phase Transitions* **55**, 79–126.

Brown, W. L. & Parsons, I. 1994 Feldspars in igneous rocks. In *NATO ASI, Feldspars and their reactions* (ed. I. Parsons) (Edinburgh, 29/6–10/7/1993), pp. 449–500.

Capponi, J. J. *et al.* 1987 Structure of the 100 K superconductor $Ba_2YCu_3O_7$ between (5÷300) K by neutron powder diffraction. *Europhys. Lett.* **3**, 1301–1307.

Carpenter, M. 1992 Thermodynamics of phase transitions in minerals: a macroscopic approach. In *The stability of minerals.* London: Chapman & Hall.

Chrosch, J. & Salje, E. K. H. 1994 Thin domain walls in $YBa_2Cu_3O_{7-\delta}$ and their rocking curves. An X-ray diffraction study. *Physica* **225C**, 111–116.

Drake, A., Hirst, P. J., Aindow, M. & Abell, J. S. 1994 Growth and microstructure of aluminium substituted $YBa_2Cu_3O_{7-\delta}$ single crystals. In *IOP Conf. Series: Electron Microscopy and Analysis Group Conf.* (Liverpool, 14/9–17/9/1993), pp. 333–336.

Gerdanian, P. & Picard, C. 1993 Some experimental evidence concerning the location of the OI–OII phase boundary in $YBa_2Cu_3O_z$. *Physica* **204C**, 419–424.

Hayward, S. A. & Salje, E. K. H. 1996 Displacive phase transition in anorthoclase: the 'plateau effect' and the effect of t_1/t_2 ordering on the transition temperature. *Am. Mineral.* **81**, 1332–1336.

Hirst, P. J., Drake, A., Rand, M. & Abell, J. S. 1994 The microstructure of the twin to tweed transition in aluminium substituted $YBa_2Cu_3O_{7-\delta}$ single crystals. *Physica* **235C**, 371–372.

Hirst, P. J., Abell, J. S., Locherer, K. R., Chrosch, J. & Salje, E. K. H. 1996 (In preparation.)

INEL 1985 *Inel reference manual.* Instrumentation électronique.

Jiang, X., Wochner, P., Moss, S. C. & Zschak, P. 1991 Diffuse X-ray scattering study of an oxygen-disordered tetragonal $YBa_2(Cu_{0.955}Al_{0.045})_3O_7$ crystal. *Phys. Rev. Lett.* **67**, 2167–2170.

Jiang, X., Wochner, P., Moss, S. C. & Zschack, P. 1992 Diffuse X-ray scattering study of oxygen-disordered tetragonal $YBa_2(Cu_{1-x}Al_x)_3O_7$ crystals. In *Proc. Int. Conf. on Martensitic Transformations* (Monterey, CA, 20/7–24/7/1992), pp. 731–736.

Jorgensen, J. D., Veal, B. W., Paulikas, A. P. *et al.* 1990 Structural properties of oxygen-deficient $YBa_2Cu_3O_{7-\delta}$. *Phys. Rev.* B **41**, 1863–1877.

Kartha, S., Krumhansl, J. A., Sethna, J. P. & Wickham, L. K. 1995 Disorder-driven pretransitional tweed pattern in martensitic transformations. *Phys. Rev.* B **52**, 803–822.

Kistenmacher, T. 1988 Substitution for copper in $YBa_2Cu_3O_y$: the first 3%. *Phys. Rev.* B **38**, 8862–8867.

Kromann, R., Bilde-Sørensen, J. B., de Reus, R., Vase, P., Andersen, N. H. & Freltoft, T. 1992 Relation between critical current densities and epitaxy of $YBa_2Cu_3O_7$ thin films on MgO(100) and $SrTiO_3$(100). *J. Appl. Phys.* **71**, 3419–3426.

Lacayo, G., Kästner, G. & Herrmann, R. 1992 Twin to tweed transition in $YBa_2Cu_3O_{7-\delta}$ by substitution of Al for Cu. *Physica* **192C**, 207–214.

Landau, L. D. & Lifshitz, E. M. 1980 *Statistical physics*, 3rd edn, vol. 1. New York: Pergamon.

Parlinski, K., Salje, E. K. H. & Heine, V. 1993*a* Annealing of tweed microstructure in high T_c superconductors studied by a computer simulation. *Acta Metall. Mater.* **41**, 839–847.

Parlinski, K., Heine, V. & Salje, E. K. H. 1993*b* Origin of tweed texture in the simulation of a cuprate superconductor. *J. Phys.* C **5**, 497–518.

Putnis, A. & Salje, E. K. H. 1994 Tweed microstructures: experimental observations and some theoretical models. *Phase Transitions* **48**, 85–105.

Roth, G., Ewert, D., Heger, G., Hervieu, M., Michel, C., Raveau, B., D'Yvoire, F. & Revcolevschi, A. 1987 Phase-transformation and microtwinning in crystals of the high-T_c superconductor $YBa_2Cu_3O_{8-x}$, x-congruent-to-1.0. *Z. Phys.* B **69**, 21–27.

Salje, E. K. H. 1990 *Phase transitions in ferroelastic and co-elastic crystals.* Cambridge University Press.

Salje, E. K. H. 1995 Chemical mixing and structural phase transitions: the plateau effect and oscillatory zoning near surfaces and interfaces. *Eur. J. Mineral.* **7**, 791–807.

Salje, E. K. H. & Parlinski, K. 1991 Microstructures in high T_c superconductors. *Supercond. Sci. Technol.* **4**, 93–97.

Salje, E. K. H., Wruck, B. & Thomas, H. 1991 Order-parameter saturations and low-temperature extension of Landau theory. *Z. Phys.* B **82**, 399–404.

Sapriel, J. 1975 Domain-wall orientations in ferroelastics. *Phys. Rev.* B **12**, 5128–5140.

Schleger, P. *et al.* 1995*a* Observation of ortho-III correlations by neutron and hard X-ray scattering in an untwinned $YBa_2Cu_3O_{6.77}$ single crystal. *Physica* **241C**, 103–110.

Schleger, P. *et al.* 1995*b* Random-field structural transition in $YBa_2Cu_3O_{6.5}$? *Phys. Rev. Lett.* **74**, 1446–1449.

Schmahl, W. W. *et al.* 1989 Twin formation and structural modulations in orthorhombic and tetragonal $YBa_2(Cu_{1-x}Co_x)_3O_{7-\delta}$. *Phil. Mag. Lett.* **60**, 241–248.

Semenovskaya, S. & Kachaturyan, A. G. 1991 Kinetics of strain-related morphology transformation in $YBa_2Cu_3O_{7-\delta}$. *Phys. Rev. Lett.* **67**, 2223–2226.

Semenovskaya, S. & Kachaturyan, A. G. 1992 Secondary and tertiary ordering in non-stochiometric $YBa_2Cu_3O_{6+\delta}$. *Phil. Mag. Lett.* **66**, 105–114.

Semenovskaya, S. & Kachaturyan, A. G. 1993 Structure transformations in $YBa_2Cu_3O_{6+\delta}$ caused by oxygen ordering. *Physica* **66D**, 205–222.

Semenovskaya, S., Zhu, Y., Suenaga, M. & Khachaturyan, A. G. 1993 Twin and tweed microstructures in $YBa_2Cu_3O_{7-\delta}$ doped by trivalent cations. *Phys. Rev.* B **47**, 12 182–12 189.

Smith, J. V. 1974 *Feldspar minerals: chemical and textural properties*, vol. 1. Berlin: Springer.

Steinborn, T., Miehe, G., Wiesner, J. *et al.* 1994 Twinning of $YBa_2Cu_3O_7$ thin films on different substrates and modifications by irradiation. *Physica* **220C**, 219–226.

Tsatskis, I., Vul, DA., Salje, E. K. H. & Heine, V. 1994 Geometrical coupling between inhomogeneous strain fields: application to fluctuations in ferroelastics. *Phase Transitions* **52**, 95–107.

Van Tendeloo, G., Zandbergen, H. W. & Amelinckx, S. 1987 Electron-diffraction and electron-microscopic study of Ba–Y–Cu–O superconductingfs materials. *Solid State Commun.* **63**, 389–393.

Van Tendeloo, G., Broddin, D., Zandbergen, H. W. & Amelinckx, S. 1990 Detwinning mechanism, twinning dislocations and planar defects in $YBa_2Cu_3O_{7-\delta}$. *Physica* **167C**, 627–639.

Van Tendeloo, G., Krekels, K., Amelinckx, S. *et al.* 1995 Structural investigations of recently discovered high T_c superconductors. *Microscopy Res. Technique* **30**, 102–122.

Vul, D. A., Tsatskis, I. & Salje, E. K. H. 1995 On the possibility of equilibrium tweed microstructure in tetragonal $YBa_2Cu_3O_7$ superconductors. *Phil. Mag. Lett.* **72**, 277–284.

Wadhawan, V. K. 1988 Epitaxy and disorientations in the ferroelastic superconductor $YBa_2\ Cu_3O_{7-x}$. *Phys. Rev.* B **38**, 8936–8939.

Yeadon, M., Aindow, M., Wellhöfer, F. & Abell, J. S. 1993 TEM and STM studies of growth spirals on laser-ablated epitaxial $YBa_2Cu_3O_{7-\delta}$. In *IOP Conf. Series: Electron Microscopy and Analysis Group Conf.* (Liverpool, 14/9–17/9/1993), pp. 283–286.

Yeadon, M., Hirst, P. J., Locherer, K. R., Chrosch, J., Abell, J. S., Aindow, M., Wellhöfer, F., Woodall, P. & Salje, E. K. H. 1995 Investigation of the influence of Al-doping on the microstructures of laser-ablated epitaxial $YBa_2Cu_3O_{7-\delta}$ thin films on (001) MgO. In *IOP Conf. Series: Electron Microscopy and Analysis Group Conf.* (Birmingham 1995), pp. 421–424.

Yeadon, M., Hirst, P. J., Locherer, K. R., Chrosch, J., Abell, J. S., Aindow, M., Wellhöfer, F. & Salje, E. K. H. 1996 The effects of Al substitution on the microstructure and properties of laser-ablated epitaxial $YBA_2Cu_3O_{7-\delta}$ films on (001) MgO. *Physica.* C (In the press.)

Xu, Y., Suenaga, M., Tafto, J. *et al.* 1989 Microstructure, lattice parameters, and superconductivity of $YBa_2\ (Cu_{1-x}Fe_x)_3O_{7-\delta}$ for $0 \leqslant x \leqslant 0.33$. *Phys. Rev.* B **39**, 6667–6679.

Zhu, Y. & Cowley, J. 1994 Three-dimensional structural modulation in doped $YBa_2Cu_3O_{7-\delta}$. *Phil. Mag.* A **69**, 397–408.

Zhu, Y., Suenaga, M. & Moodenbaugh, A. R. 1990 Displacement wave of the tweed structure in Y–Ba–Cu–O oxides. *Phil. Mag. Lett.* **62**, 51–59.

Zhu, Y., Suenaga, M. & Moodenbaugh, A. R. 1991 Oxygen, diffuse scattering, and tweed structure in the $YBa_2Cu_3O_{7-\delta}$ system. *Ultramicroscopy* **37**, 341–350.

Zhu, Y., Suenaga, M. & Tafto, J. 1993 Interpretation of tweed contrast from the $YBa_2Cu_3O_{7-\delta}$ system. *Phil. Mag.* A **67**, 573–583.

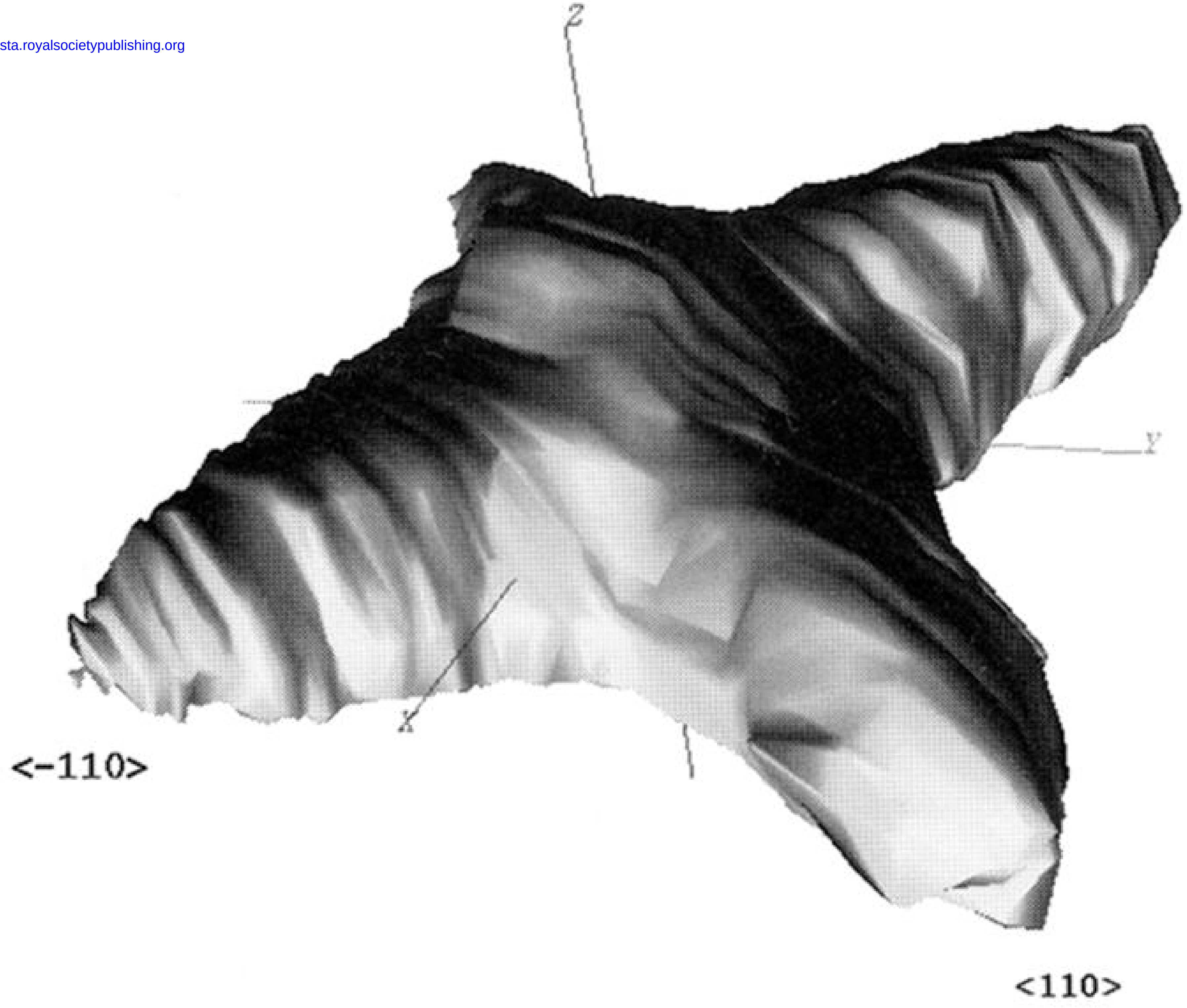

gure 12. An isosurface representation of the (200)/(020) reflection for a single crystal doped ith $x = 0.04$ aluminium. The value of equal intensity is about a hundredth of the maximum the centre. Axis range is $(-0.006, -0.006, -0.006)$–$(0.006, 0.006, 0.006)$ in Å^{-1}.

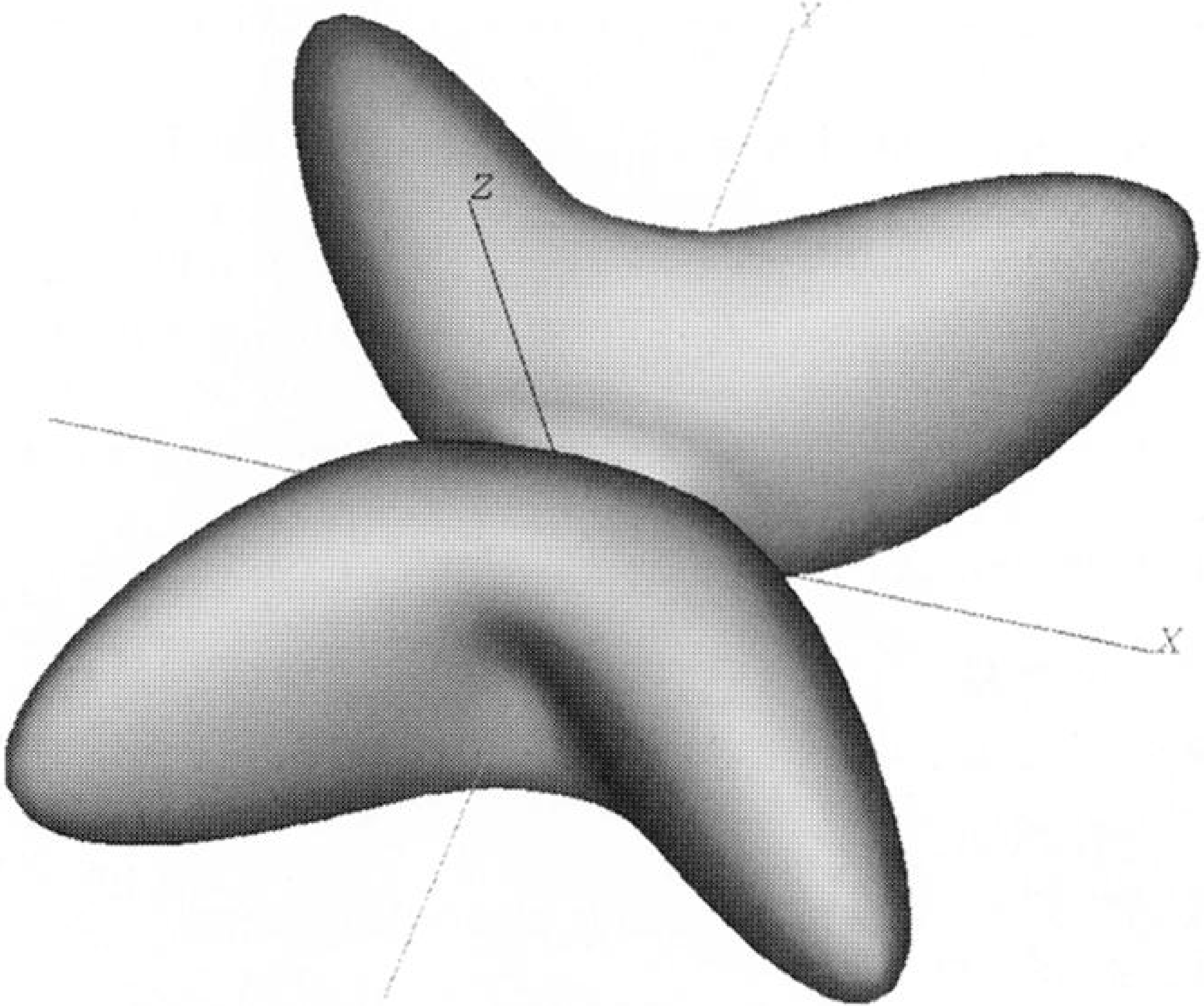

gure 14. Isosurface plot of the diffuse scattering generated by calculating the static displacements in $YBa_2Cu_3O_{7-\delta}$.

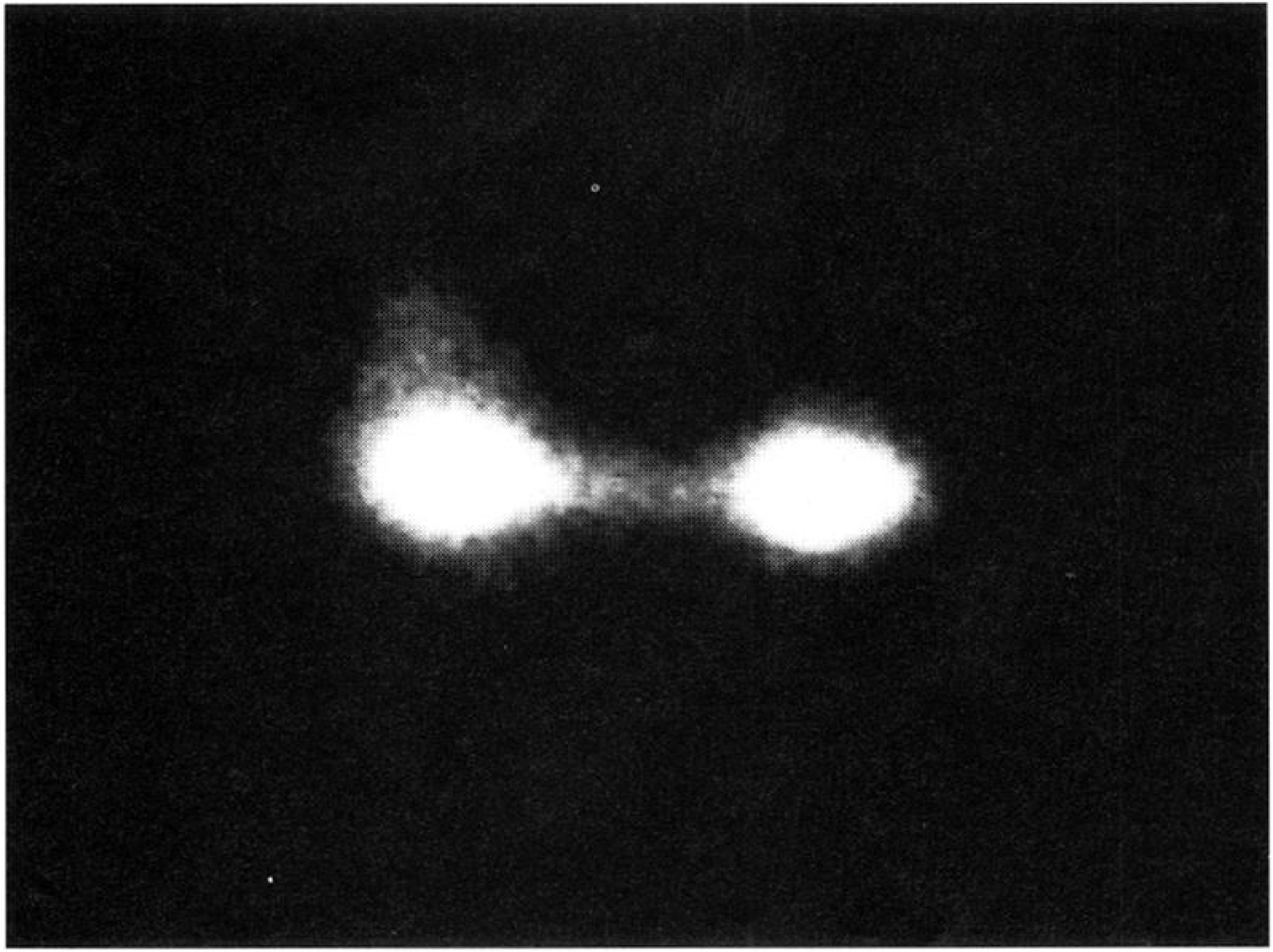

gure 22. Electron diffraction pattern showing twin-related diffraction peaks in anorthoclase and diffuse streaks due to walls in between.

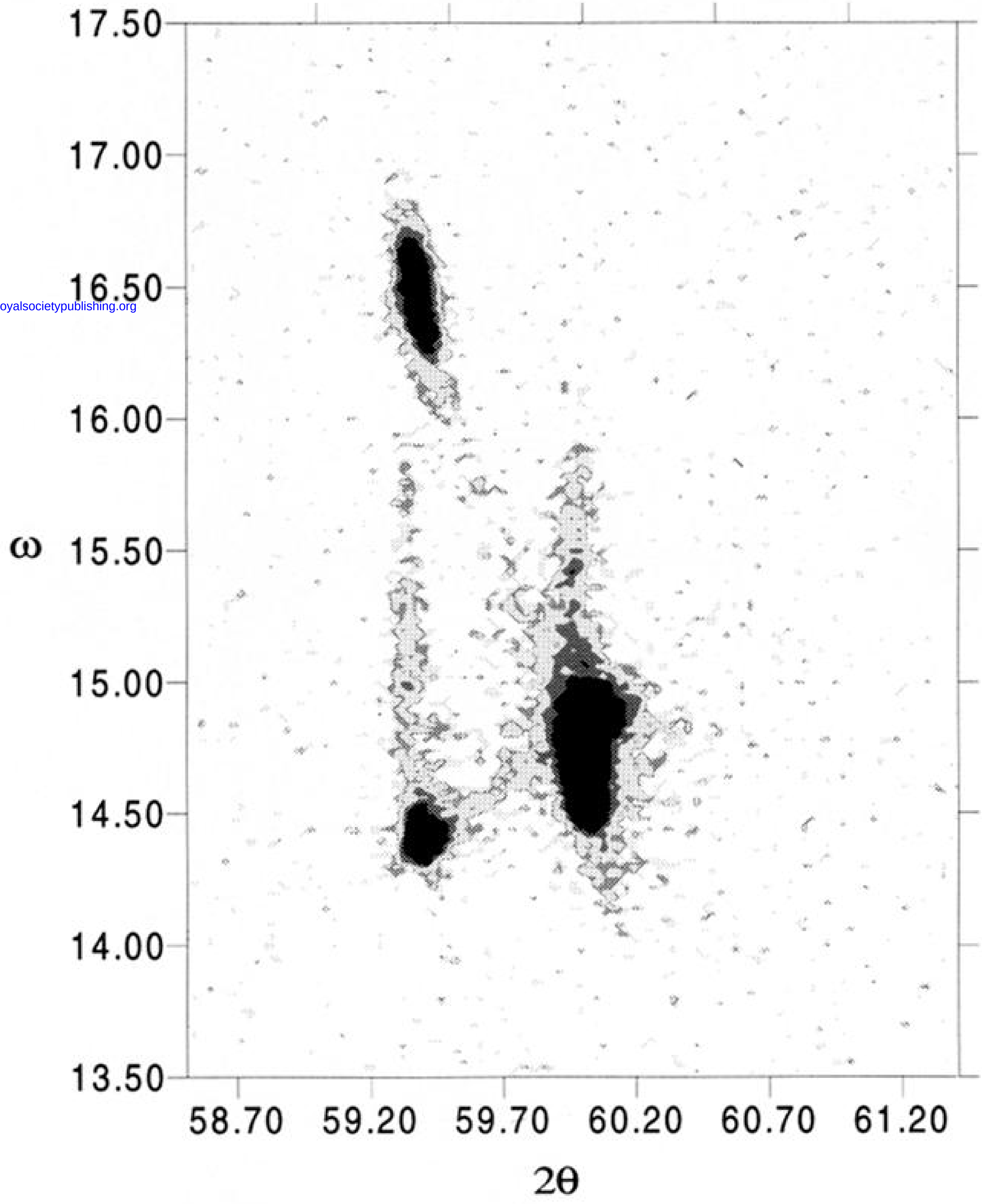

igure 23. Plot of intensity versus 2θ and ω of experimental diffraction data for anorthoclase sample at 623 K. ω is the angle of incidence between the X-ray beam and (010).

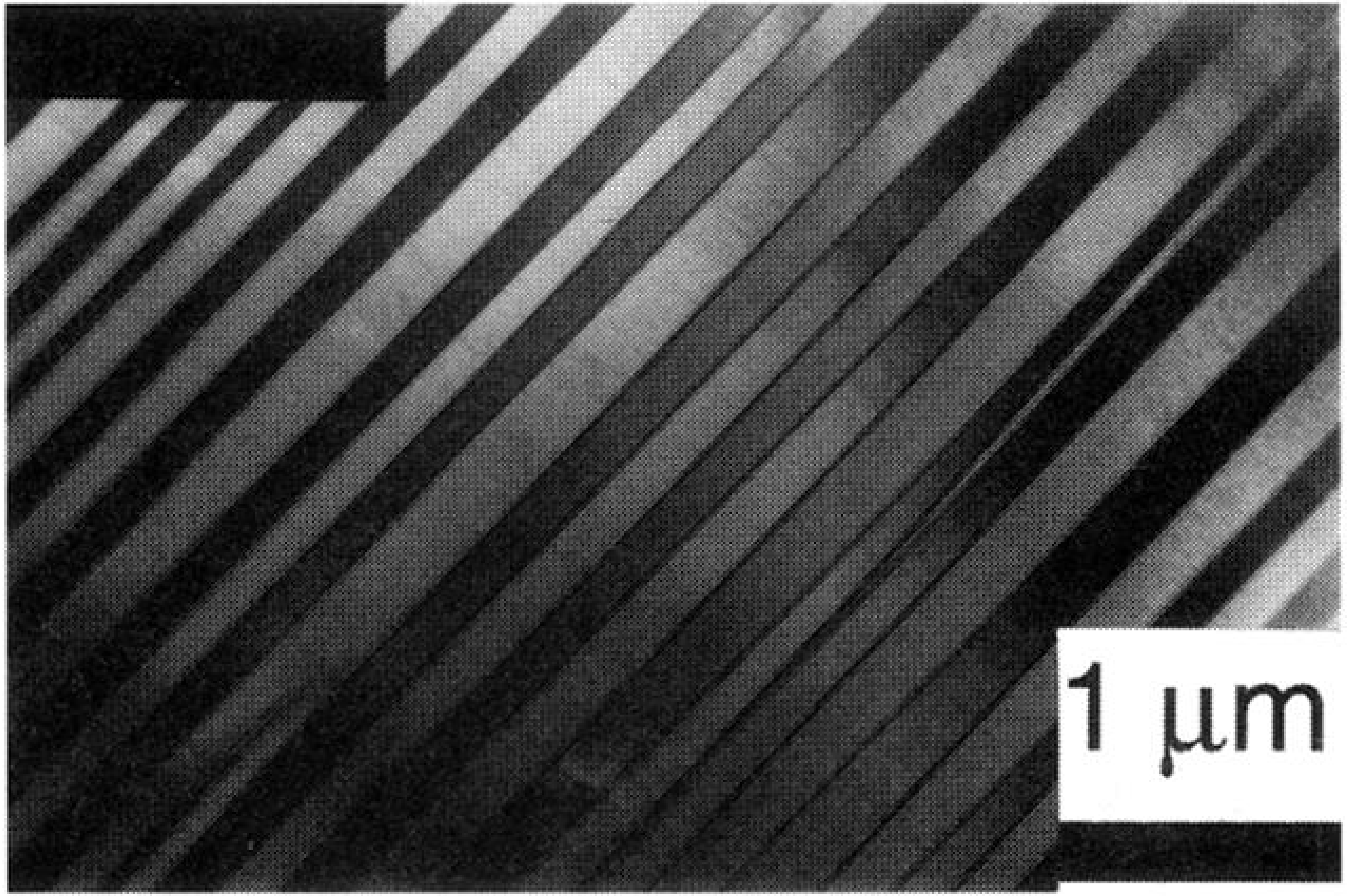

gure 24. One of the electron micrographs used to estimate twin density in anorthoclase.